

## Three-dimensional Structure of Incomplete Carbon-Oxygen Detonations in Type Ia Supernovae

A. KHOKHLOV,<sup>1</sup> I. DOMÍNGUEZ,<sup>2</sup> A. Y. CHTCHELKANOVA,<sup>3</sup> P. HOEFlich,<sup>4</sup> E. BARON,<sup>5,6</sup> K. KRISCIUNAS,<sup>7</sup> M. PHILLIPS,<sup>8</sup> N. SUNTZEFF,<sup>7</sup> AND L. WANG<sup>7</sup>

<sup>1</sup>*Department of Astronomy and Astrophysics, the Enrico Fermi Institute, and the Computational Institute, The University of Chicago, Chicago, IL 60637, USA*

<sup>2</sup>*Departamento de Física Teórica y del Cosmos, University of Granada, 18071 Granada, Spain*

<sup>3</sup>*U.S. National Science Foundation, 2415 Eisenhower Ave Alexandria, VA 22314, USA*

<sup>4</sup>*Department of Physics, Florida State University, Tallahassee, FL 32306, USA*

<sup>5</sup>*Planetary Science Institute, 1700 East Fort Lowell Road, Suite 106, Tucson, AZ 85719-2395 USA*

<sup>6</sup>*Hamburger Sternwarte, Gojenbergsweg 112, 21029 Hamburg, Germany*

<sup>7</sup>*George P. and Cynthia Woods Mitchell Institute for Fundamental Physics & Astronomy, Texas A&M University, Department of Physics & Astronomy, 4242 TAMU, College Station, TX 77843, USA*

<sup>8</sup>*Las Campanas Observatory, Carnegie Observatories, Casilla 601, La Serena, Chile*

(Received today; Revised today; Accepted today)

Submitted to The Astrophysical Journal

### ABSTRACT

Carbon-oxygen (CO) detonation with reactions terminating either after burning of C<sup>12</sup> in the leading C<sup>12</sup> + C<sup>12</sup> reaction or after burning of C<sup>12</sup> and O<sup>16</sup> to Si-group elements may occur in the low-density outer layers of exploding white dwarfs and be responsible for the production of intermediate-mass elements observed in the outer layers of Type Ia supernovae. Basic one-dimensional properties of CO-detonations have been summarized in our previous work. This paper presents the results of two- and three-dimensional numerical simulations of low-density CO-detonations and discusses their multidimensional stability, cellular structure, and propagation through a constant low-density background. We find three-dimensional CO detonations to be strikingly different from their one-dimensional and two-dimensional counterparts. Three-dimensional detonations are significantly more robust and capable of propagating without decay compared to highly unstable and marginal one- and two-dimensional detonations. The detonation cell size and whether burning of C<sup>12</sup> in a three-dimensional detonation wave is followed by the subsequent O<sup>16</sup> burning is sensitive to both the background density and the initial C<sup>12</sup> to O<sup>16</sup> mass ratio. We also discuss the possible implications for understanding the observed early time bumps in light-curves.

*Keywords:* hydrodynamics - instabilities - nuclear reactions, nucleosynthesis, abundances - shock waves - supernovae: general - white dwarfs

### 1. INTRODUCTION

Thermonuclear supernovae, so-called Type Ia supernovae (SNe Ia), are the explosive destruction of CO white dwarfs (WDs) in binary or triple systems. They produce at least 50% of the iron-group elements in the Universe, are laboratories of modern and plasma physics (Hoyle & Fowler 1960), and provide a yardstick for modern cosmology.

The extraordinary discoveries in cosmology overshadow the diversity of SNe Ia that has emerged in recent years, leading to three main explosion scenarios (Hoeftlich & Khokhlov 1996). The first of these considers a surface He detonation (HeD) that triggers a detonation of a sub-Chandrasekhar mass (sub- $M_{\text{Ch}}$ ) WD with a low-density CO core (Woosley et al.

1980; Nomoto 1982; Hoeftlich & Khokhlov 1996). A second scenario considers a delayed detonation (DD) (Khokhlov 1989a) in which the explosion of a near- $M_{\text{Ch}}$ -mass WD is triggered by compressional heating at high densities, resulting in the production of electron-capture (EC) elements. Here, the flame propagation starts as a deflagration and transitions to a detonation (Khokhlov 1989b). In the third leading scenario, two WDs merge or collide in a binary or triplet system, possibly head-on, (Webbink 1984), causing large-scale asymmetries and low-density burning.

Despite all efforts, none of the current models are based on ‘first principles’. The fact that nuclear physics determines the structure of the WD, the energy release, and the production

of elements during the explosion leads to similar spectra and light curves and causes, to first order, a ‘stellar amnesia’ of the progenitor system despite the expected potential diversity in explosions and progenitor channels.

Advances in observations during the last decades are starting to overcome the degeneracy in the solutions, but have also exposed a lack of understanding of details and the need for physical effects not considered previously, such as the cellular detonation structure in incomplete carbon burning, which is the topic of this paper. For a collection of reviews by several groups see [Alsabti & Murdin \(2017\)](#).

The outermost layers of the ejecta ( $\approx 10^{-5}$  to  $10^{-2}M_{\odot}$ ) hold a key to understanding the nature of thermonuclear SNe, the progenitor systems, and their environment. They are exposed to the emergent radiative flux during the first few days after the explosion (see Fig. 3 of [Höflich et al. 2019](#)). They involve three main components: (1) the surface layers of the exploding WD, (2) all other outer matter bound in the progenitor system, which may include a companion star, and any bound circumstellar matter (CSM) such as the accretion disc, and the inner parts of several winds (e.g., from the WD, a companion star and an accretion disc), and (3) the unbound CSM consisting of the outer faster and less dense parts of the winds and the interstellar medium.

Only with recent advances in time-domain astronomy, specific features related to the surface layers have been observed. These include early bumps in the light curves and colors ([Marion et al. 2016](#); [Hosseinzadeh et al. 2017](#); [Contreras et al. 2018](#); [Dimitriadis et al. 2019](#); [Shappee et al. 2019](#); [Burke et al. 2022a,b](#); [Deckers et al. 2022](#); [Hosseinzadeh et al. 2022](#); [Ni et al. 2023a,b](#); [Wang et al. 2024](#)) and the early blue-red-blue evolution ([Ni et al. 2023a](#); [Hosseinzadeh et al. 2022](#)) which may be understood in terms of additional energy deposition due to interaction with the outer matter or to nuclear burning during the breakout ([Höflich & Schaefer 2009](#); [Perley et al. 2022](#); [Hosseinzadeh et al. 2022](#)), or as the result of expansion effects ([Ashall et al. 2022](#); [Höflich et al. 1993](#)), or, like in SN 2021aefx, a result of an off-center delayed detonation transition (DDT) ([Ni et al. 2023a](#)). Moreover, early-time polarization spectra of SN 2019np revealed a large asymmetry, but with fluctuating polarization spectra hinting at the existence of small-scale instabilities with scales of  $1000 \text{ km s}^{-1}$  that may be attributed to inhomogeneous nuclear burning products ([Höflich et al. 2023](#)).

The work presented here focuses on the surface layers of the WD. Note that surface burning of He can be expected both in double-detonations of sub- $M_{Ch}$  mass WDs triggered by He-detonation ([Buckley et al. 2021](#)) and in the surface H/He rich layers of near  $M_{Ch}$  mass WDs triggered by an outgoing detonation front ([Höflich & Schaefer 2009](#); [Höflich et al. 2019](#)). What is missing in the literature are multi-dimensional simulations corresponding to the properties found close to the

WD surface. Three previous studies, done in two-dimensions, were performed in the context of nearly Chandrasekhar mass explosions of SNe Ia, although they focused on larger densities at which the transition from deflagration to detonation is expected to occur,  $\approx 10^7 \text{ g cm}^{-3}$  ([Boisseau et al. 1996](#); [Gamezo et al. 1999](#); [Timmes et al. 2000](#)). These two-dimensional studies paved the way for our three-dimensional simulations, identifying the relevance of the transverse waves and cellular structures, and analyzing the needed resolution and dependence on initial conditions. Recently, a work by [Iwata & Maeda \(2024\)](#), submitted to ApJ, has also presented two-dimensional simulations, in this case for He-detonations in sub-Chandrasekhar SNe Ia.

In Section 2, the overall background is given for the underlying flame physics. In § 3, the problem has been formulated, and the input physics is described. In § 4, the results are presented, and in § 5 the conclusions are summarized and linked to new results in the field of SNe Ia, and the prospects are discussed.

A. Khokhlov and I. Dominguez studied instabilities under conditions of the outermost layers by an outgoing detonation wave using full 3D, high-resolution simulations covering many orders of magnitude. Employing Alexei’s code ALLA ([Khokhlov 1998](#)), the simulations are performed for subdomains between  $\approx 200$  to  $3200 \text{ km}$ .

This work was performed, and most of the paper was written prior to Alexei Khokhlov’s untimely death in 2019. Now, new observations and multidimensional simulations make it highly relevant, and it therefore has been completed by the co-authors.

## 2. BACKGROUND

It is well known that explosive CO burning in SN Ia proceeds through three distinct nuclear kinetic stages ([Thielemann et al. 1986](#); [Gamezo et al. 1999](#)). (1) *C-burning*: The  $C^{12}$  nuclei present in the initial CO mixture react and burn out in the leading  $C^{12} + C^{12}$  nuclear reaction forming such products as  $O^{16}$ ,  $Ne^{20}$ ,  $Mg^{24}$ ,  $Na^{23}$ ,  $Si^{28}$ ,  $S^{32}$ ,  $He^4$  and free neutrons and protons. (2) *O-burning*: The initial and newly formed  $O^{16}$  as well as other products of the  $C^{12} + C^{12}$  reaction burn to Si-group elements. (3) *Si-burning*: The nuclei of the Si-group burn into the Fe-peak nuclei, where the matter reaches a state of nuclear statistical equilibrium (NSE). For the conditions that occur in SNe Ia, the time scales of the above three stages,  $t_C$ ,  $t_O$  and  $t_{Si}$ , respectively, are vastly different,  $t_C \ll t_O \ll t_{Si}$ , and their absolute values are a strong function of temperature or, alternatively, of the background density at which burning takes place. The cause of the density-dependence of the reaction timescales is the decrease of the specific heat of degenerate matter with increasing density, which translates into an increase of the burning temperature.

Densities at which different stages of CO burning take place in a SN Ia may be roughly estimated by comparing the nuclear kinetic time scales with the hydrodynamic timescale of a white dwarf explosion,  $t_h \simeq 1$  s. By equating  $t_C$ ,  $t_O$  and  $t_{Si}$  to  $t_h$  one finds that Si-burning in SN Ia occurs at densities  $\rho > 10^7$  g cm $^{-3}$ , O-burning at densities  $10^6 < \rho < 10^7$  g cm $^{-3}$ , and C-burning at  $10^4 < \rho < 10^6$  g cm $^{-3}$ . Within the framework of current hydrodynamical models the above property of CO-burning gives a general explanation of one of the most important observational properties of SN Ia - the presence of Fe-peak elements in the inner parts of a supernova where burning is able to proceed to NSE, and the presence of intermediate mass elements in the outer layers where burning is incomplete (Khokhlov 1991).

While a general SN Ia scenario relies on the above mentioned well established basic thermodynamic and nuclear kinetic properties of degenerate CO matter and a basic hydrodynamical timescale of the exploding carbon-oxygen WD, details of hydrodynamical models depend on many factors which are still not fully understood, such as the exact initial exploding configuration, details of the deflagration stage, mechanism(s) of the initiation of a detonation wave and a deflagration-to-detonation transition, multi-dimensional propagation of detonation waves, etc. Current full-star simulations of SN Ia explosions do not have sufficient numerical resolution to resolve the real structure of a detonation wave, and the level of input physics to model these important processes is not sufficiently well known.

Detonations occurring at densities below  $10^6$  g cm $^{-3}$  are especially important for the interpretation of early observations of SNe Ia before maximum light, which are accumulating rapidly. At these densities, the detonation may involve only the first stage of carbon burning. Hereafter, such detonations are referred to as incomplete or C-detonations. They are the main focus of this study. In our previous paper (Domínguez & Khokhlov 2011), we dealt with one-dimensional properties of C-detonations. This paper presents the results of two- and three-dimensional numerical simulations of C-detonations. Our multi-dimensional simulations show that properties of the same detonation wave are strikingly different when it propagates in one, two, or three dimensions. This paper combines and summarizes the results of our one-, two- and three-dimensional simulations, explains the role of dimensionality in the propagation of the detonation waves, considers different background densities and initial chemical compositions, and discusses the implications of the results to SN Ia modeling.

### 3. FORMULATION OF THE PROBLEM

#### 3.1. Equations and input physics

To describe a detonation wave we use time-dependent, compressible, reactive flow Euler equations of fluid dynamics,

$$\frac{\partial \rho}{\partial t} + \nabla \cdot (\rho \mathbf{u}) = 0, \quad (1)$$

$$\frac{\partial \rho \mathbf{u}}{\partial t} + \nabla \cdot (\rho \mathbf{u} \mathbf{u}) + \nabla P = 0, \quad (2)$$

$$\frac{\partial E}{\partial t} + \nabla \cdot (\mathbf{u}(E + P)) = \rho \dot{q}, \quad (3)$$

$$\frac{\partial \rho \mathcal{Y}}{\partial t} + \nabla \cdot (\rho \mathbf{u} \mathcal{Y}) = \rho \mathcal{R}, \quad (4)$$

where  $\rho$  is mass density,  $\mathbf{u}$  is velocity,  $E = \rho(\epsilon + \frac{u^2}{2})$  is energy density,  $\epsilon$  is internal energy per unit mass, and  $\mathcal{Y} = \{\mathcal{Y}_1, \dots, \mathcal{Y}_N\}$  are mole concentrations of reactants.  $\mathcal{R} = \{\mathcal{R}_1, \dots, \mathcal{R}_N\}$  are the corresponding net reaction rates which are functions of  $\mathcal{Y}$ ,  $\rho$ , and temperature  $T$ . The nuclear energy generation rate is taken to be

$$\dot{q} = \mathbf{Q} \cdot \mathcal{R} = \sum_{i=1}^N Q_i \mathcal{R}_i, \quad (5)$$

where  $\mathbf{Q} = \{Q_1, \dots, Q_N\}$  are the binding energies of nuclei.

Nuclear kinetics is described by a network which consists of  $N = 13$  nuclei He $^4$ , C $^{12}$ , O $^{16}$ , Ne $^{20}$ , Mg $^{24}$ , Si $^{28}$ , S $^{32}$ , Ar $^{36}$ , Ca $^{40}$ , Ti $^{44}$ , Cr $^{48}$ , Fe $^{52}$ , and Ni $^{56}$ . The network takes into account reactions between  $\alpha$ -particles and heavier nuclei C $^{12} + \alpha \leftrightarrow$  O $^{16} + \gamma$ , O $^{16} + \alpha \leftrightarrow$  Ne $^{20}$ , ..., Fe $^{52} + \alpha \leftrightarrow$  Ni $^{56}$ ; binary reactions C $^{12} + C^{12}$ , C $^{12} + O^{16}$ , O $^{16} + O^{16}$  and the triple-alpha reaction  $3\alpha \leftrightarrow$  C $^{12} + \gamma$ . Effective  $(\alpha, \gamma)$  reaction rates are calculated as sums of contributions from  $(\alpha, p)(p, \gamma)$ ,  $(\alpha, n)(n, \gamma)$ , and  $(\alpha, \gamma)$  reaction channels involving protons, neutrons, and photons ( $p$ ,  $n$ , and  $\gamma$ , respectively). Forward reaction rates and partition functions are taken from compilations of Fowler et al. (1978); Woosley et al. (1978); Thielemann (1993). Screening corrections are applied to forward reactions (Yakovlev & Shalybkov 1989), while reverse reactions are calculated from the principle of detailed balance using ion chemical potentials with liquid-phase Coulomb corrections to account for screening of reverse reactions (Yakovlev & Shalybkov 1989). While not mentioned, the same screening corrections were used in the calculations of (Domínguez & Khokhlov 2011). The network captures the multi-stage nature of explosive CO burning and correctly reproduces the time-scales of C, O, and Si burning stages. For densities,  $\rho_0 \leq 10^6$  g cm $^{-3}$ , burning in SNe Ia does not proceed to Fe-group elements. In these conditions, the network can be truncated. We verified that a less expensive eight-species  $\alpha$ -network truncated at Ar $^{36}$  provides the same results as a complete  $\alpha$ -network. The eight-species network was used in most of the simulations. The equation of state includes contributions from the ideal Fermi-Dirac electrons

and positrons with arbitrary degeneracy and relativism, equilibrium Planck radiation, and Boltzmann nuclei (similar to Timmes & Swesty (2000) and originally based in Nadyozhin (1974)). Some details and a comparison with our previous approximations are discussed in Appendix B.

### 3.2. Numerical method and computational setup

Equations (1) - (4) are solved using an adaptive mesh refinement (AMR) reactive-flow fluid dynamic simulation code ALLA (Khokhlov 1998). The code uses a directionally split Godunov-type second-order accurate conservative algorithm for solving the Euler part of the equations. Numerical fluxes are evaluated using a monotone linear reconstruction and a Riemann solver. The code uses a dynamic cell-by-cell adaptive mesh refinement. The mesh can be characterized by minimum and maximum levels of refinement,  $l_{min}$  and  $l_{max}$ , in all simulations we used four levels of refinement,  $l_{min} = l_{max} - 3$ . At refinement level,  $l$ , the computational cell size is  $\Delta x(l) = L/2^l$ , where  $L$  is the size of a computational domain. The mesh is dynamically refined around shocks, contact discontinuities, and in regions of large gradients of density, pressure, and composition of  $\text{He}^4$ ,  $\text{C}^{12}$ ,  $\text{O}^{16}$ ,  $\text{Ne}^{20}$ ,  $\text{Mg}^{24}$  and  $\text{Si}^{28}$ . Shocks and discontinuities are always refined to a maximum level (for details see Section 6, Mesh refinement, in Khokhlov (1998)). The operator-split approach is used for coupling hydrodynamic and nuclear kinetic algorithms. A method of integration of stiff equations of  $\alpha$ -network nuclear kinetic is described in Appendix B. The current version of the code, ALLA/HSCD, runs in a hybrid OpenMP/MPI mode on up to  $\sim 10^5$  cores (we acknowledge Mr. C. Bacon and the staff of the ALCF at the Argonne National Laboratory for their contribution with the code development and scaling).

Three-dimensional simulations are performed in a rectangular computational domain (“tube”) with length  $L$  and square cross-section  $W^2$  (Fig. 1). Steady-state Zeldovich-Neumann-Döring (ZND) detonation solutions are used as initial conditions. The ZND detonation consists of a planar leading shock followed by a one-dimensional reaction zone. In a reference frame moving with the detonation velocity, all parameters inside the ZND reaction zone are a function of a distance from the shock,  $x$ , and do not depend on time. ZND solutions are calculated as described in (Domínguez & Khokhlov 2011) and interpolated onto a computational domain with the leading shock placed at  $x = 0.9L$  and facing the right X-boundary. Simulations are performed in a reference frame moving with the ZND detonation velocity in order to keep the wave inside the tube. A constant supersonic inflow of unburned matter with velocity  $-D$ , where  $D$  is the detonation velocity, is imposed on the right boundary and a zero gradient outflow is imposed on the left X-boundary. Symmetry boundary conditions are used in Y and Z-directions. Errors of interpolation introduce longitudinal perturbations

into initial conditions. A small initial spherical temperature perturbation is added behind the leading shock in order to trigger transverse instabilities.

### 3.3. Characteristic scales and numerical resolution

A half-reaction length,  $x_C$ , of a ZND detonation is used in the paper as a characteristic spatial scale. It is defined as a distance from the leading shock to a point where half of the initial  $\text{C}^{12}$  is consumed. The corresponding temporal scale, the ZND half-reaction time, is  $t_C = \int_0^{x_C} u(x)^{-1} dx$ , where  $u(x)$  is the fluid velocity relative to the shock. The spatial resolution of a simulation can be characterized in a density-independent way by the number of computational cells of level  $l_{max}$  per half-reaction length scale,

$$n_c = \frac{x_C}{\Delta x(l_{max})}. \quad (6)$$

The Courant condition on a hydrodynamical time step can then be written as

$$\Delta t = CFL \cdot \frac{\Delta x(l_{max})}{\max(a_s + |u|)} = CFL \cdot \frac{x_C}{n_c \max(a_s + |u|)}. \quad (7)$$

CFL is the Courant-Friedrichs-Lewy factor or Courant factor (Courant et al. 1928), and  $a_s$  is the velocity of sound. Since  $t_C \approx x_C/a_s$  it follows that  $t_C/\Delta t \approx n_c$  when  $CFL \approx 1$ . Thus, spatially resolving the reaction zone with the accuracy  $\approx x_C/n_c$  leads to temporal resolution of the reaction zone with the similar accuracy  $\approx t_C/n_c$ . In the simulations, we used  $CFL = 0.7$  and  $n_c = 12.3 - 49$  (Table 2).

## 4. RESULTS

### 4.1. Input parameters

Simulations were performed for freely propagating Chapman-Jouguet (CJ) detonations. A CJ detonation is characterized by the minimum possible detonation velocity,  $D_{CJ}$ , the lowest postshock temperature,  $T_s$ , and the largest  $x_C$  and  $t_C$  scales as compared to overdriven detonations with velocities  $D > D_{CJ}$  (see i.e. Lee (2008) and Fickett & Davis (1979)). Note that here we refer to CJ C-detonation with reduced energy release, not to a CJ complete detonation, in which burning proceeds to NSE (see subsection 3.3 in Domínguez & Khokhlov (2011)). We considered two mixture compositions, a  $0.5 \text{C}^{12} + 0.5 \text{O}^{16}$  and a  $0.3 \text{C}^{12} + 0.7 \text{O}^{16}$  mixture by mass. The  $0.5 \text{C}^{12} + 0.5 \text{O}^{16}$  mixture is representative of the outer layers of a WD that reaches the Chandrasekhar mass, accreting H or He from the companion star (single degenerate scenario). In this case, the C/O ratio is expected to be  $\geq 0.5$  due to radiative shell He burning. The  $0.3 \text{C}^{12} + 0.7 \text{O}^{16}$  mixture represents a case when the exploding WD is formed by merging of two WD (double degenerate scenario). In this case, the CO accreted matter comes in part from the previous convective He burning core, which is

carbon-depleted (Domínguez et al. 2001, 2003; Bravo et al. 2010). Parameters of CJ detonations used as initial conditions for multi-dimensional simulations are listed in Table. 1 and Fig. 2 gives the corresponding half-reaction thickness,  $x_C$ , as a function of initial density  $\rho_0$  for the two mixture composition considered,  $X_C^{12} = 0.5$  and  $0.3$ .

#### 4.2. Three-dimensional detonation wave

Table 2 summarizes three-dimensional simulations for the  $0.5\text{C}^{12} + 0.5\text{O}^{16}$  composition. Simulations are referenced with background density,  $\rho_0$ , followed by an alpha-numerical label. For example, 1e6C1 in Tab. 2 indicates a run C1 at  $\rho_0 = 10^6\text{ g cm}^{-3}$ . For each run, the table gives the length and width of the computational domain, minimum and maximum levels of refinement, the numerical resolution, and the location of the initial spherical perturbation. The obtained results do not depend on the initial perturbations, the boundary conditions, or the size of the computational domain (see also Boisseau et al. (1996) & Gamezo et al. (1999)).

As was explained in Sect 3.2 each simulation started with the initially planar one-dimensional ZND detonation wave plus a small spherical temperature perturbation introduced behind the leading shock. A typical development of a multi-dimensional structure of a detonation wave starting from such initial conditions is illustrated in Fig. 3 for case 1e6C2. At the beginning of the simulation, the planar wave starts to decay due to a strong one-dimensional longitudinal instability. However, the perturbation introduced behind the leading shock generates a spherical shock wave that propagates towards the leading shock and side walls. Reflections off the walls create additional secondary shocks, which interact with each other and with the leading shock. The interactions rapidly trigger a train of transverse reaction waves traveling in orthogonal directions behind the leading shock.

Fig. 3a shows the reflection of a first transverse wave from the bottom wall and two additional transverse waves traveling toward the upper wall. An unaffected part of the planar detonation wave close to the upper wall is still decaying. In the orthogonal cross-section (Fig. 3b) the two transverse waves created by the interaction of the spherical shock with the leading shock have not yet reached the boundaries. The transverse reaction waves accelerate burning behind the leading shock and prevent the decay of the detonation wave. Instead of decaying, the detonation wave settles into a quasi-steady cellular regime of propagation.

The cellular detonation regime is well known (Lee 1984; Shepherd 2009) and is schematically illustrated in two dimensions in Fig. 4. The leading shock of a cellular detonation is not one-dimensional and consists of sections of varying strength, which are joined at triple points with transverse waves moving behind the leading shock. The matter that passes through the leading shock burns in narrow reaction

zones behind the strong sections of the shock and accumulates in thick layers behind the weak sections of the shock. This matter is subsequently burned in transverse waves periodically passing through the layers. Collisions of transverse waves moving in opposite directions create new strong sections of the leading shock, whereas previous strong sections weaken with time. The picture continuously evolves with time and periodically repeats itself. Trajectories of triple points form rhomboidal shapes called detonation cells. In narrow tubes, the detonation wave may be affected by the walls. In wide tubes, like those used in these simulations, and in unconfined detonations, the cell size,  $l_c$ , depends on the intrinsic kinetic and thermodynamic properties of matter.

The above description is highly idealized. Real detonations are three-dimensional. Strong and weak sections of the leading shock are surfaces, and triple points are triple lines. A regular cellular structure depicted in Fig. 4 is only typical of weakly unstable detonations. With increasing instability, the cellular structure becomes irregular and chaotic. In addition, interactions of secondary waves with the leading shock and with each other generate shear layers, vortical motions, and turbulence. The relevance of vorticity was first discussed in Timmes et al. (2000) for larger densities.

The onset of a cellular regime in all simulations occurred approximately after  $\approx 2 - 3$  sound crossing times of the tube width. After that, the detonation propagates in a fully developed cellular regime with the detonation velocity very close to its Chapman-Jouguet value,  $D \approx D_{CJ}$ . The simulations show an irregular cellular propagation of a detonation wave in all three-dimensional runs. As an example, Figs. 5–7 show the cellular structure of the detonation wave in run 1e6C2 at  $t = 50t_c$ . At this time, the detonation is in a fully developed cellular regime and initial conditions are virtually forgotten.

Strong and weak parts of the leading shock are clearly visible in the temperature plot Fig. 5a. The temperature is as low as  $\approx 1.5 \times 10^9\text{ K}$  behind weak parts of the shock and reaches  $\approx 4.0 \times 10^9\text{ K}$  behind the strong parts. The steady-state post-shock temperature is  $T_s = 2.27 \times 10^9\text{ K}$ , so that temperature fluctuations behind the leading shock are of the order  $\approx 2$ . Transverse waves are clearly visible on the pressure plot in Fig. 5b. The waves are stronger inside the layers of shocked, unburned matter where they are essentially transverse detonation waves. The waves continue as transverse shocks in burned matter away from the leading shock. Pressure behind the transverse waves in burned matter varies by a factor of  $\approx 2$ .

Fluctuations of thermodynamical parameters lead to variations of chemical composition of the burned matter. Fig. 6 shows order  $\approx 100\%$  fluctuations of  $\text{C}^{12}$  and  $\text{Si}^{28}$  mass fractions close behind the leading shock. Fig. 7 shows transversal components of fluid velocity. Fluctuations of the velocity components on average, are of the order  $\delta \approx \pm 3 \times 10^8\text{ cm s}^{-1}$

or  $\approx \pm 0.5a_s$ . The largest fluctuations reach  $\approx a_s$ . Close inspection of the results shows that fluctuations are partially associated with the instantaneous location of transverse waves and represent the post-shock fluid velocity. Another component of the velocity fluctuations is associated with shear layers, interactions of shock waves with density inhomogeneities, and shock-shock interactions. The two components of the velocity field are of the same order.

Fig. 8 compares a YZ-averaged three-dimensional structure of run 1e6C2 at  $t = 50t_c$  with the corresponding steady-state ZND detonation. The figure shows that the averaged three-dimensional structure closely resembles the steady-state one-dimensional reaction zone. The only difference is that  $C^{12}$  is incinerated in a three-dimensional detonation slightly more rapidly, and slightly more  $Si^{28}$  is produced. While slowly decreasing in amplitude, the variations of pressure, temperature, and velocity around the average values persist in burned matter long after the matter passes through the leading shock. The velocity structures and transverse waves are present behind the leading shock at distances  $\approx 20 - 30x_c$  and more. The same is true for chemical non-uniformities of Si, Ne, Mg and other products of C-burning, although the compositional non-uniformities are typically less than 50% of the average and diminish with the distance from the shock. Compositional non-uniformities of  $C^{12}$  rapidly burn out and are generally confined within a short distance  $\approx 5x_c$  from the leading shock. Virtually no carbon remains at  $x > 5x_c$ . Overall, the three-dimensional detonation appears very robust. Similar behavior was found in all other three-dimensional simulations.

#### 4.3. Detonation cells

Fig. 9 shows a side view Schlieren image of run 1e6C2 detonation at the same moment of time as in Figs. 5-7. Both the leading shock and multiple transverse waves are visible, but due to a large number of transverse waves, the estimation of the characteristic cell size  $l_c$  is impossible. To estimate  $l_c$  we use the head-on  $S_x$  Schlieren images. Figs. 9a-d show  $S_x$  images of a fully developed cellular detonation for runs 1e6C2, 1e6C1, 1e6C, and 1e6D, respectively. The first three simulations are performed using the same width  $W = 20.8x_c$  and three different numerical resolutions,  $n_c = 12.3, 24.5$  and  $49.0$ . The last simulation is done at the lowest resolution  $n_c = 12.3$  resolution, but inside a two times wider computational domain,  $W = 41.7x_c$ . Fig. 9d shows one-quarter of the YZ-cross section.

With increasing resolution, we observe a finer and more detailed structure of transverse waves. The figure shows that the cellular structure is rather chaotic, but irregular detonation cells are discernible. On average, one can identify  $\approx 3 - 4$  detonation cells across the width of the computational domain. The cells seem to be slightly larger at the lowest resolution

but are practically the same at the two higher resolutions. From the simulations, we roughly estimate  $l_c \approx 5x_c$ . The results obtained at different numerical resolutions indicate that the numerical resolution does not significantly affect the estimation of  $l_c$ . The independence of  $l_c$  from the tube width confirms that the width of the computational domain is sufficient, and tube geometry does not affect the cell size. The cell size estimated from the simulations is the intrinsic cell size of an unconfined freely propagating CJ detonation.

Fig. 10 compares the cell structure of detonations propagating at different densities,  $\rho_0 = 5 \times 10^5, 7 \times 10^5$  and  $1 \times 10^6 \text{ g cm}^{-3}$ . The half-reaction length of the detonation is a strong function of  $\rho_0$  and varies from highest to lowest density by more than an order of magnitude (Table 1). To compare detonations at different  $\rho_0$  the  $S_x$  images were scaled to the same relative size. The comparison shows a remarkable similarity between the detonation cells at various densities. The relation between the detonation cell size and the half-reaction length of a ZND detonation, is  $l_c \approx 5x_c$  and holds for all densities.

#### 4.4. Two-dimensional detonation

Simulations show a striking difference in the propagation of two-dimensional detonation waves as compared to a propagation of the same detonations in three dimensions. Instead of developing a robust small-scale cellular structure, two-dimensional detonations are characterized by quasi-periodic episodes during which the leading shock weakens and separates from the reaction zone. The layer of accumulated unburnt fuel is then incinerated by a transverse detonation wave, which bounces off the sides of the computational domain.

As an example, Fig. 11 shows the propagation of a two-dimensional detonation in a  $0.5C^{12} + 0.5O^{16}$  mixture at  $\rho_0 = 10^6 \text{ g cm}^{-3}$ . The computational setup and numerical resolution for this calculation are exactly the same as for the three-dimensional run 1e6C2, except that the third dimension is eliminated. In Fig. 11a one can see a layer of unburned fuel accumulating behind the leading shock (light blue). A transverse wave just bounced off the lower boundary and created a section of a highly overdriven detonation propagating to the right (red). With time, the overdriven detonation weakens, and the reaction zone separates from the shock. Fig. 11b shows the newly formed layer of unburned fuel (light blue) being incinerated in a transverse wave that bounced off the upper boundary. A new section of an overdriven detonation created by the bounce is visible near the upper boundary (red). The process repeats itself, roughly, on a timescale  $t_{2D} \approx 2W/a_s$  where  $a_s$  is the sound speed in shocked matter. However, the process is not strictly periodic. From time to time, the entire cross-section may be briefly filled with an overdriven detonation, but the detonation eventually weakens and decays. One of these ‘‘overdriven’’ episodes is shown in Fig. 11c. Similar

behavior was found in calculations with increased numerical resolution.

The period increases with increasing  $W$  until a certain width is reached where re-initiation of a detonation begins to take place, not only at the boundaries but also in the middle of the computational domain, creating an additional transverse detonation wave moving behind the leading shock. Re-initiation in the middle of the domain via the Zeldovich gradient mechanism associated with the temperature non-uniformities has long been suggested, and may lead to a re-ignition. However, our simulations lack the needed resolution to resolve the gradients.

Note that previous two-dimensional simulations of CO detonation in degenerate matter obtained a clear cellular structure, in most cases for higher background densities than the case shown here, as they focused on the delayed detonation transition density,  $\approx 10^7 \text{ g cm}^{-3}$ . In particular, [Boisseau et al. \(1996\)](#) assumed a background initial density of  $3 \times 10^7 \text{ g cm}^{-3}$ , [Gamezo et al. \(1999\)](#) explored a range of densities, from  $10^6 \text{ g cm}^{-3}$  to  $3 \times 10^7 \text{ g cm}^{-3}$ , discussing in detail the  $5 \times 10^6 \text{ g cm}^{-3}$  case, [Timmes et al. \(2000\)](#) studied the  $10^7 \text{ g cm}^{-3}$  case, while [Iwata & Maeda \(2024\)](#) have included, in their He detonation simulations, a C detonation at  $10^6 \text{ g cm}^{-3}$ . In all these studies the initial carbon mass fraction was 0.5, except in [Timmes et al. \(2000\)](#) that assumed 1.0. Only [Gamezo et al. \(1999\)](#) and [Iwata & Maeda \(2024\)](#) studied densities as low as our  $10^6 \text{ g cm}^{-3}$  case.

A basic difference between these two studies and our two-dimensional example, all done at the same initial density, is the energy release. In our incomplete C-detonations is 0.37 MeV/nuc, which is a factor of  $\approx 2$  smaller than that of a complete or NSE-detonation, 0.76 MeV/nuc. Thus,  $x_C$  is above two and one order of magnitudes greater than those obtained in [Gamezo et al. \(1999\)](#) and [Iwata & Maeda \(2024\)](#), respectively.

In our simulation, the spontaneous re-initiation of a detonation may reflect the intrinsic properties of an unconfined two-dimensional detonation, and thus the minimal value of  $W$  when this happens may represent the spatial scale of a two-dimensional detonation cell,  $l_{c,2D}$ . We find that  $l_{c,2D}$  is significantly larger than the size of a three-dimensional detonation cell,  $l_{c,2D} \approx 50l_c$ . This size is much greater than that obtained by other authors, taking  $x_C$  as a reference, we obtain  $\approx 250 x_C$ , compared to  $\approx 30 x_C$  and  $\approx 10 x_C$  obtained by [Gamezo et al. \(1999\)](#) and [Iwata & Maeda \(2024\)](#), respectively.

#### 4.5. Effect of the composition

3-D simulations show the sensitivity of the detonation burning on the abundances or, more precisely, the C/O ratio in the regime of distributed burning. In Figs. 12, 13 and 14, the evolution of the detonation is shown at  $t=92, 143,$  and  $226 t_c$  for the same parameters of model 1e6C2 with  $\rho_c = 10^6 \text{ g cm}^{-3}$ ,

but a mixture of 0.3 C and 0.7 O. The result is qualitatively different from the case of C/O=1 ([Khokhlov & Dominguez 2015](#)). The average post-shock temperature in detonations with  $X_C^{12} = 0.3$  is lower compared to a detonation with  $X_C^{12} = 0.5$  due to a lower energy release, 0.22 and 0.37 MeV/nucleon, respectively, in the leading C12 + C12 reaction. As a result the detonation zone is more unstable and is characterized by a higher amplitude of temperature fluctuations. The peak temperature near the triple-points becomes so high that the shock collisions trigger O-burning which converts matter to Si-group elements and almost doubles the energy release. A forward and backward O-detonation develops, so the O-burning quickly spreads through the reaction zone. The results are few inhomogeneities remaining of C and O and a reduction of layers produced by incomplete carbon burning.

Thus, in C-rich mixtures,  $X_C^{12} \geq 0.5$ , the detonation propagates as a quasi-steady detonation but in carbon poor mixtures,  $X_C^{12} \leq 0.3$ , the detonation must be treated in a fully non-stationary manner ([Khokhlov & Dominguez 2015](#)).

In close to  $M_{Ch}$  mass explosions, assuming accretion of H/He rich matter from a companion, and that the whole WD is completely mixed before the explosion, the average  $X_C^{12}$  is expected to range from above 0.4 to 0.5 (C/O from above 0.6 to 1), depending on initial mass and metallicity. Note that  $X_C^{12}$  could be much larger if the outer layers are not mixed.

While, for secular and dynamical mergers, lower  $X_C^{12}$  may be expected, from above 0.3 to 0.4 (C/O from above 0.4 to 0.7), depending on initial WD masses and metallicities. This is due just to the fact that two WDs, instead of one, contribute with the C-poor material coming from the central convective He-burning stellar phase. Central He-burning is a long phase, in which there is enough time for alpha captures on  $C^{12}$ , thus, decreasing  $C^{12}$  and producing  $O^{16}$  ([Domínguez et al. 2001, 2003; Bravo et al. 2010; Khokhlov et al. 2012; Piersanti et al. 2019](#)).

## 5. DISCUSSION AND CONCLUSIONS

This paper presents results of three-dimensional numerical simulations of CO-detonations in a tube with physical and chemical properties similar to the outer layers of SNe Ia. We study the impact of dimensionality comparing with two- and three-dimensional numerical simulations. We also analyze the results assuming different background densities and chemical mixtures.

- Three-dimensional detonations appear very robust in all the simulations. The detonation cells are very similar at the different studied densities, 0.5 to  $1 \times 10^6 \text{ g cm}^{-3}$ . All show detonation cell sizes above 5 times the carbon half-reaction length,  $x_C$  (which is defined as the distance from the leading shock to a point where half of initial  $C^{12}$  is consumed).

- The average three-dimensional structure resembles the steady-state one-dimensional reaction zone. The most remarkable differences are that  $C^{12}$  is burnt slightly more rapidly and slightly more  $Si^{28}$  is produced in the three-dimensional models.
- In the three-dimensional simulations, non-uniformities of products of C-burning, like Si, Ne or Mg, are present at up to 20-30  $x_C$  of the leading shock, while C non-uniformities rapidly burn out and remain closer to the leading shock, within 5  $x_C$ , with no C at further distances.
- Multidimensional simulations show that properties of the same detonation are strikingly different when it propagates in three-dimensions and in two-dimensions. We find that in two-dimensional simulations, instead of developing a robust small-scale cellular structure, the leading shock weakens and separates periodically from the reaction zone. This behavior is caused by the intrinsic instability of a C-detonation to longitudinal perturbations. The estimated detonation cell sizes are above 50 times larger than in three-dimensional simulations. Two-dimensional simulations may over-predict the abundances of intermediate mass elements and of residual  $C^{12}$ . Thus, two-dimensional models of Type Ia supernovae involving detonation waves need to be re-investigated using three-dimensional simulations.
- This dependence of the problem on the dimensionality suggests that the outcome of incomplete detonations in SNe Ia should depend on the geometry of the exploding star which may depend on the progenitors, on the direction of the propagation with respect to the density gradients, and/or whether it is deformed by rotation.
- We find incomplete C-detonations to be highly unstable. To treat a detonation as a quasi-steady wave, two conditions must be fulfilled: (a) large separation of the half-reaction spatial scales of C, O and Si-burning, and (b) sufficient stability to avoid the transition to an O-detonation. The first condition is usually met in C-detonations when the C abundance mass fraction  $\geq 0.5$ , while we find the second to be violated in carbon poor mixtures.
- If carbon abundance  $X_C^{12} \leq 0.3$  a rapid transition to O-detonation occurs. This is due to the increasing instability of the incomplete carbon detonation due to the lower carbon abundance and lower energy release. The amplitude of the temperature fluctuations increases exponentially with the  $\beta$  parameter (see Domínguez & Khokhlov 2011) for the stability study, being  $\beta=16.6$  in our 0.5C + 0.5O model, and 20 for the 0.3C + 0.7O

model. Thus, chemical composition of the outer layers plays a crucial role in the explosions. In SNe Ia, initial low carbon abundance closed to the surface is expected when two or three WDs are involved as progenitors. Note that the final masses of the exploding WDs could be sub-Chandrasekhar or nearly Chandrasekhar. In these cases little or no oxygen will remain in the outer layers after the explosion. While an initial rich carbon outer zone, expected when H/He is accreted and converted to CO, would finally show larger oxygen abundances.

- Chemical inhomogeneities are rapidly burned away in the region of explosive oxygen burning because the burning time scales are shorter than the expansion time scales. However, the burning time scales become larger in layers of incomplete carbon burning, and will ‘freeze’ out in the outer layers.
- Mapping the computational domain of the simulations into the layers with incomplete carbon-burning of spherical explosion models (Hoeflich et al. 2019, their Fig. 3), final expansion velocities of  $\approx 20,000\text{--}30,000$   $\text{km s}^{-1}$  are exposed in the ejecta during the first few days after the explosion. The scales of the inhomogeneities correspond to about  $1000$   $\text{km s}^{-1}$ .
- Cellular instabilities can be expected in the entire C-layers and affect the flame propagation. However, the chemical inhomogeneities are burned away at layers with higher densities because the hydrodynamical time scales for the explosion are larger than the burning time scales  $t_c$ .
- The results of inhomogeneities is a ‘picket-fence’ structure consisting of burned and unburned layers. The result is an increase in the luminosity when the photosphere passes the corresponding layers (Aldoroty et al. 2023). Early bumps in the LCs and polarization spectra coincide with the low-density domain and may be caused by chemical inhomogeneities, as discussed in Sect. 1.
- Recently, the mechanism of turbulent deflagration-to-detonation transition has been established (Poludnenko et al. 2019). However, the current study may also be relevant to detonation initiation, including multi-spot DDTs, since critical conditions for initiation and for the DDT correlate with basic properties of the detonation waves.

In summary, the modeling of low density incomplete detonation in SNe Ia, especially in low carbon matter as may result when two or three WDs are involved as progenitors, requires



time-dependent, three-dimensional reactive flow simulations with numerically-resolved C and O-burning zones.

This work establishes detonation instabilities and cell structure as important ingredients in the physics of thermonuclear supernovae. Now, models, including density gradients and full radiation-hydrodynamics or radiation-magnetic-hydrodynamics simulations (Remming & Khokhlov 2014; Hristov et al. 2018), are needed.

**Acknowledgements:** The co-authors are grateful to Alexei for many years of collaboration and friendship. The work was carried out within the NSF project “Collaborative re-

search: Three-Dimensional Simulations of Type Ia Supernovae: Constraining Models with Observations” supported by the NSF grant AST-0709181; I.D acknowledges funding from the project PID2021-123110NB-I00 financed by the Spanish MCIN/AEI /10.13039/501100011033/ & FEDER A way to make Europe, UE, and the Spanish Ministry for Education Mobility Programme within the framework of the National Plan I+D+I 2008-2013. We thank the staff of the ALCF at the Argonne National Laboratory, especially Mr. C. Bacon (ALCF), for their help with the code development.

## REFERENCES

- Aldoroty, L., Wang, L., Hoefflich, P., et al. 2023, *ApJ*, 948, 10, doi: [10.3847/1538-4357/acad78](https://doi.org/10.3847/1538-4357/acad78)
- Alsabti, A. W., & Murdin, P. 2017, *Handbook of Supernovae* (Berlin: Springer), doi: [10.1007/978-3-319-21846-5](https://doi.org/10.1007/978-3-319-21846-5)
- Ashall, C., Lu, J., Shappee, B. J., et al. 2022, *ApJL*, 932, L2, doi: [10.3847/2041-8213/ac7235](https://doi.org/10.3847/2041-8213/ac7235)
- Boisseau, J. R., Wheeler, J. C., Oran, E. S., & Khokhlov, A. M. 1996, *ApJL*, 471, L99, doi: [10.1086/310338](https://doi.org/10.1086/310338)
- Bravo, E., Domínguez, I., Badenes, C., Piersanti, L., & Straniero, O. 2010, *ApJL*, 711, L66, doi: [10.1088/2041-8205/711/2/L66](https://doi.org/10.1088/2041-8205/711/2/L66)
- Buckley, D. A. H., Bagnulo, S., Britto, R. J., et al. 2021, *MNRAS*, 506, 4621, doi: [10.1093/mnras/stab1791](https://doi.org/10.1093/mnras/stab1791)
- Burke, J., Howell, D. A., Sand, D. J., & Hosseinzadeh, G. 2022a, *arXiv e-prints*, arXiv:2208.11201, doi: [10.48550/arXiv.2208.11201](https://doi.org/10.48550/arXiv.2208.11201)
- Burke, J., Howell, D. A., Sand, D. J., et al. 2022b, *arXiv e-prints*, arXiv:2207.07681, doi: [10.48550/arXiv.2207.07681](https://doi.org/10.48550/arXiv.2207.07681)
- Contreras, C., Phillips, M. M., Burns, C. R., et al. 2018, *ApJ*, 859, 24, doi: [10.3847/1538-4357/aabaf8](https://doi.org/10.3847/1538-4357/aabaf8)
- Courant, R., Friedrichs, K., & Lewy, H. 1928, *Mathematische Annalen*, 100, 32, doi: [10.1007/BF01448839](https://doi.org/10.1007/BF01448839)
- Deckers, M., Maguire, K., Magee, M. R., et al. 2022, *MNRAS*, 512, 1317, doi: [10.1093/mnras/stac558](https://doi.org/10.1093/mnras/stac558)
- Dimitriadis, G., Foley, R. J., Rest, A., et al. 2019, *ApJL*, 870, L1, doi: [10.3847/2041-8213/aaedb0](https://doi.org/10.3847/2041-8213/aaedb0)
- Domínguez, I., Höflich, P., & Straniero, O. 2001, *ApJ*, 557, 279, doi: [10.1086/321661](https://doi.org/10.1086/321661)
- . 2003, *Mem. Soc. Astron. Italiana*, 74, 938
- Domínguez, I., & Khokhlov, A. 2011, *ApJ*, 730, 87, doi: [10.1088/0004-637X/730/2/87](https://doi.org/10.1088/0004-637X/730/2/87)
- Fickett, W., & Davis, C. 1979, *Detonation* (Los Alamos Series in Basic and Applied Sciences, Berkeley: University of California Press)
- Fowler, W. A., Woosley, S. E., & Engelbrecht, C. A. 1978, *ApJ*, 226, 984, doi: [10.1086/156679](https://doi.org/10.1086/156679)
- Gamezo, V. N., Wheeler, J. C., Khokhlov, A. M., & Oran, E. S. 1999, *ApJ*, 512, 827, doi: [10.1086/306784](https://doi.org/10.1086/306784)
- Hoefflich, P., & Khokhlov, A. 1996, *ApJ*, 457, 500, doi: [10.1086/176748](https://doi.org/10.1086/176748)
- Hoefflich, P., Ashall, C., Fisher, A., et al. 2019, in *Nuclei in the Cosmos XV*, Vol. 219, 187–194, doi: [10.1007/978-3-030-13876-9\\_31](https://doi.org/10.1007/978-3-030-13876-9_31)
- Hoefflich, P., Yang, Y., Baade, D., et al. 2023, *MNRAS*, 520, 560, doi: [10.1093/mnras/stad172](https://doi.org/10.1093/mnras/stad172)
- Höflich, P., Mueller, E., & Khokhlov, A. 1993, *A&A*, 268, 570
- Höflich, P., & Schaefer, B. E. 2009, *ApJ*, 705, 483, doi: [10.1088/0004-637X/705/1/483](https://doi.org/10.1088/0004-637X/705/1/483)
- Hosseinzadeh, G., Sand, D. J., Valenti, S., et al. 2017, *ApJL*, 845, L11, doi: [10.3847/2041-8213/aa8402](https://doi.org/10.3847/2041-8213/aa8402)
- Hosseinzadeh, G., Sand, D. J., Lundqvist, P., et al. 2022, *ApJL*, 933, L45, doi: [10.3847/2041-8213/ac7cef](https://doi.org/10.3847/2041-8213/ac7cef)
- Hoyle, F., & Fowler, W. A. 1960, *ApJ*, 132, 565, doi: [10.1086/146963](https://doi.org/10.1086/146963)
- Hristov, B., Collins, D. C., Hoefflich, P., Weatherford, C. A., & Diamond, T. R. 2018, *ApJ*, 858, 13, doi: [10.3847/1538-4357/aab7f2](https://doi.org/10.3847/1538-4357/aab7f2)
- Iwata, K., & Maeda, K. 2024, *arXiv e-prints*, arXiv:2412.15580, doi: [10.48550/arXiv.2412.15580](https://doi.org/10.48550/arXiv.2412.15580)
- Khokhlov, A. 1999, YASS, Yet Another Stiff Solver that works, Naval Research Laboratory Technical Memorandum Reports
- Khokhlov, A., & Domínguez, I. 2015, in *ICDERS*, Vol. 297, Proceedings of the 25th International Colloquium on the Explosion of Reactive Systems, 113.07
- Khokhlov, A., Domínguez, I., Bacon, C., et al. 2012, in *Astronomical Society of the Pacific Conference Series*, Vol. 453, Advances in Computational Astrophysics: Methods, Tools, and Outcome, ed. R. Capuzzo-Dolcetta, M. Limongi, & A. Tornambè, 107
- Khokhlov, A. M. 1989a, *MNRAS*, 239, 785, doi: [10.1093/mnras/239.3.785](https://doi.org/10.1093/mnras/239.3.785)
- . 1989b, *MNRAS*, 239, 785
- . 1991, *A&A*, 245, 114
- . 1998, *Journal of Computational Physics*, 143, 519, doi: [10.1006/jcph.1998.9998](https://doi.org/10.1006/jcph.1998.9998)

- Lee, J. H. S. 1984, *Ann. Rev. Fluid Mech.*, 16, 311–336
- . 2008, *The Detonation Phenomenon*
- Marion, G. H., Brown, P. J., Vinkó, J., et al. 2016, *ApJ*, 820, 92, doi: [10.3847/0004-637X/820/2/92](https://doi.org/10.3847/0004-637X/820/2/92)
- Nadyozhin, D. 1974, *Nauchn. Inf.*, 32, 3
- Ni, Y. Q., Moon, D.-S., Drout, M. R., et al. 2023a, *ApJ*, 959, 132, doi: [10.3847/1538-4357/ad0640](https://doi.org/10.3847/1538-4357/ad0640)
- . 2023b, *ApJ*, 946, 7, doi: [10.3847/1538-4357/aca9be](https://doi.org/10.3847/1538-4357/aca9be)
- Nomoto, K. 1982, *ApJ*, 257, 780, doi: [10.1086/160031](https://doi.org/10.1086/160031)
- Oran, E. S., & Boris, J. P. 2000, *Numerical Simulation of Reactive Flow*
- Perley, D. A., Sollerman, J., Schulze, S., et al. 2022, *ApJ*, 927, 180, doi: [10.3847/1538-4357/ac478e](https://doi.org/10.3847/1538-4357/ac478e)
- Piersanti, L., Yungelson, L. R., Cristallo, S., & Tornambé, A. 2019, *MNRAS*, 484, 950, doi: [10.1093/mnras/stz033](https://doi.org/10.1093/mnras/stz033)
- Poludnenko, A. Y., Chambers, J., Ahmed, K., Gamezo, V. N., & Taylor, B. D. 2019, *Science*, 366, aau7365, doi: [10.1126/science.aau7365](https://doi.org/10.1126/science.aau7365)
- Remming, I. S., & Khokhlov, A. M. 2014, *ApJ*, 794, 87, doi: [10.1088/0004-637X/794/1/87](https://doi.org/10.1088/0004-637X/794/1/87)
- Shappee, B. J., Holoiien, T. W. S., Drout, M. R., et al. 2019, *ApJ*, 870, 13, doi: [10.3847/1538-4357/aac79](https://doi.org/10.3847/1538-4357/aac79)
- Shepherd, J. 2009, *Proceedings of the Combustion Institute*, 32, 83
- Thielemann, F. 1993, private communication
- Thielemann, F. K., Nomoto, K., & Yokoi, K. 1986, *A&A*, 158, 17
- Timmes, F. X., & Swesty, F. D. 2000, *ApJS*, 126, 501, doi: [10.1086/313304](https://doi.org/10.1086/313304)
- Timmes, F. X., Zingale, M., Olson, K., et al. 2000, *ApJ*, 543, 938, doi: [10.1086/317135](https://doi.org/10.1086/317135)
- Wang, Q., Rest, A., Dimitriadis, G., et al. 2024, *ApJ*, 962, 17, doi: [10.3847/1538-4357/ad0edb](https://doi.org/10.3847/1538-4357/ad0edb)
- Webbink, R. F. 1984, *ApJ*, 277, 355, doi: [10.1086/161701](https://doi.org/10.1086/161701)
- Woosley, S. E., Fowler, W. A., Holmes, J. A., & Zimmerman, B. A. 1978, *Atomic Data and Nuclear Data Tables*, 22, 371, doi: [10.1016/0092-640X\(78\)90018-9](https://doi.org/10.1016/0092-640X(78)90018-9)
- Woosley, S. E., Weaver, T. A., & Taam, R. E. 1980, in *Texas Workshop on Type I Supernovae*, ed. J. C. Wheeler, 96–112
- Yakovlev, D. G., & Shalybkov, D. A. 1989, *Sov. Sci. Rev. E. Astrophysics and Space Physics*, 7, 311

## APPENDIX

## A. VISUALIZATION

Two-dimensional fields of physical variables are presented using a standard color palette, represented by a color bar in each figure. Color bars in each figure are marked with a scale variable,  $c$ , which ranges from zero to one,  $0 \leq c \leq 1$ . A displayed physical variable, say,  $f$ , is related to  $c$  as

$$f = f_{min} + c \cdot (f_{max} - f_{min}), \quad c = \frac{f - f_{min}}{f_{max} - f_{min}}, \quad (\text{A1})$$

where  $f_{min}$  and  $f_{max}$  are the minimum and maximum values of  $f$ . They are listed in figure captions. For example, in Fig. 5a the range of temperature is  $T = \{0 - 4 \times 10^9\}$  K. The correspondence between  $T$  and  $c$  is then  $T = 4 \times 10^9 \cdot c$ . In Fig. 5b the correspondence between pressure  $P$  and  $c$  is  $\lg(P) = 22.0 + 2.0 \cdot c$ .

Numerical Schlieren images are used to visualize three-dimensional fields with large density gradients, such as shocks, reaction fronts, and contact discontinuities. The images are generated by an absolute value of a component of a density gradient orthogonal to a viewing direction along the line of sight (Fig. 15).

$$S_x(y, z) = \int_0^L \sqrt{\left(\frac{\partial \rho}{\partial y}\right)^2 + \left(\frac{\partial \rho}{\partial z}\right)^2} dx. \quad (\text{A2})$$

Head-on images do not detect the leading shock and provide an unobscured view of shocks and reaction fronts moving in transverse directions.

## B. STIFF INTEGRATION OF NUCLEAR KINETICS

The code uses a cell-based AMR based on a parallel fully threaded tree structure adaptive mesh refinement (AMR) reactive flow fluid dynamic code ALLA (Khokhlov 1998). Reaction terms were coupled to fluid dynamics via operator-splitting. During the hydrodynamical sub-step the Euler equations were integrated with  $\mathcal{R} = \dot{q} = 0$  using an explicit, directional-split, second-order accurate, Godunov-type conservative scheme with a Riemann solver. The time step  $\Delta t = CFL \cdot \frac{\Delta x}{a_s}$ , where  $a_s$  is the velocity of sound and  $\Delta x$  is the minimum cell size selected using a Courant number  $CFL = 0.7$ . During the chemical sub-step, the kinetic equations together with the equation of energy conservation,

$$\frac{d\mathcal{Y}}{dt} = \mathcal{R}, \quad \frac{d\epsilon}{dt} = \dot{q}, \quad \rho = const., \quad (\text{B3})$$

were integrated using a stiff solver, YASS (Yet Another Stiff Solver, developed by A. Khokhlov, Khokhlov (1999)), with adjustable sub-cycling when necessary to keep the relative accuracy of integration  $10^{-3}$  for individual species with  $\mathcal{Y}_i > 10^{-5}$ . The solver conserved the total baryon number and the sum of internal and nuclear binding energy exactly. Below, we briefly summarize its general properties.

General requirements for a numerical method for integration (1) - (4) easily follow from the analysis of temporal and spatial scales of the carbon-oxygen detonation. The temporal resolution of multi-species reactive flow simulations must be sufficient for accurately resolving critical reaction-kinetic time scales associated with the nuclear energy release and production of major nuclear species. The spatial resolution of the simulations must match their temporal resolution to account for the hydrodynamic interaction of the nuclear reactions and the fluid motions. Including networks requires a much higher temporal and spatial numerical resolution and computational resources as compared to simulation with simplified progress-variable kinetics and/or flame capturing and level-set descriptions of flame propagation. The increased temporal resolution is needed to account for a wide range of reaction time scales. The correspondingly increased spatial resolution is necessary to represent the interplay of nuclear kinetics and fluid flow properly. Typically, nuclear reaction rates vary rapidly with time and in space. For example, the  $C^{12} + C^{12}$  reaction rate is usually the highest immediately behind the detonation shock and becomes much smaller away from the shock where  $C^{12}$  has been exhausted. Therefore, the resolution requirements vary rapidly with time and space as well. This calls for an adaptive mesh refinement (AMR) approach to the simulations. AMR is able to concentrate computational resources where they are needed and to accelerate the computations significantly. Additional AMR savings come from increasing the numerical resolution near sharp features of a flow, such as shock waves, discontinuities, gradients of physical variables, and regions of high vorticity.

In this paper, we use a new massively parallel AMR code HSCD for first-principles reactive Navier-Stokes numerical simulations of high-speed combustion and detonation phenomena in terrestrial gases. The code is based on the Eulerian reactive flow AMR code ALLA, which has been used for reactive flow terrestrial and astrophysical combustion phenomena in the past (Khokhlov 1998).

Eulerian high-speed combustion and a massively parallel version with an adaptive mesh refinement immediately after each timestep are required because the simulation reaction timescales vary with spatial resolution. If  $\Delta_{t,min} \varepsilon \tau_{n,min}$  is the required temporal resolution of numerical integration associated with the shortest relevant reaction timescale ( $\tau_{n,min}$ , of reactant n), then the corresponding minimal spatial scale should be of the order  $\Delta_{x,h} \approx a_s \Delta_{t,min} \varepsilon \tau_{n,min}$ , and  $\varepsilon < 1$  is based on the consideration of the accuracy of kinetic numerical integration. For an explicit hydrodynamical code, the hydrodynamical time step  $\Delta_t$ , must be limited by the CFL stability condition,

$$\Delta_t < \Delta_{t,CFL} = \min \left( \frac{\Delta_{x,h}}{\max(a_s + |u|)} \right). \quad (\text{B4})$$

where  $u$  is the fluid velocity relative to the shock, and the maximum taken over all three directions.

Hydrodynamical simulations of SNe Ia with multi-species reaction networks, such as the  $\alpha$ -network used in this paper or more extensive networks including more species require much more computing power than simulations with simplified model networks. There are several reasons for this. One is the cost of computing nuclear kinetics. The right-hand sides of (3), (4) in this case, become much more expensive compared to those of quasi-networks. The latter may contain  $\approx 1 - 4$  pseudo-kinetic variables and have simple right-hand sides. Secondly, compared to the quasi-networks, the multi-species networks are extremely stiff. Stiffness of an  $\alpha$ -network, for example, reaches  $\approx 10^6 - 10^{13}$  in conditions of SNe Ia. As a result, the numerical integration requires unconditionally stable implicit methods and must involve evaluation of the Jacobian of the right-hand sides of the kinetic equations. This further raises the cost of kinetic integration. Such astrophysical networks are impossible to integrate using asymptotic methods (see e.g. Oran & Boris (2000)).

**Table 1.** Properties of Chapman-Jouguet C-detonations

$X_C$ <sup>(a)</sup>	$\rho_0$ <sup>(b)</sup>	$\frac{\rho_s}{\rho_0}$ <sup>(c)</sup>	$T_s$ <sup>(d)</sup>	$D_{CJ}$ <sup>(e)</sup>	$x_C$ <sup>(f)</sup>	$t_C$ <sup>(g)</sup>
0.5	0.50	4.57	2.06	0.85	$1.9 \times 10^6$	$8.6 \times 10^{-3}$
0.5	0.70	4.77	2.18	0.92	$3.6 \times 10^5$	$1.6 \times 10^{-3}$
0.5	1.00	4.35	2.27	0.87	$1.2 \times 10^5$	$5.2 \times 10^{-4}$
0.3	1.00	3.86	1.74	0.72	$2.7 \times 10^7$	$1.3 \times 10^{-1}$
0.3	3.00	3.47	1.92	0.75	$9.8 \times 10^5$	$4.2 \times 10^{-3}$
0.3	10.0	2.99	2.07	0.80	$5.0 \times 10^4$	$1.8 \times 10^{-4}$

<sup>(a)</sup> $X_C$  - initial mass fraction of  $C^{12}$ . Energy release is  $q_0 = 0.37$  MeV/nucleon and  $q_0 = 0.22$  MeV/nucleon for  $X_C = 0.5$  and  $X_C = 0.3$  compositions, respectively.

<sup>(b)</sup> $\rho_0$  - background density in  $10^6$  g cm<sup>-3</sup>.

<sup>(c)</sup> $\rho_s$  - post-shock density.

<sup>(d)</sup> $T_s$  - post-shock temperature in  $10^9$  K.

<sup>(e)</sup> $D_{CJ}$  - Chapman-Jouguet detonation velocity in  $10^9$  cm s<sup>-1</sup>.

<sup>(f)</sup> $x_C$  - half-reaction length of a detonation in cm.

<sup>(g)</sup> $t_C$  - half-reaction time of a detonation in sec.

**Table 2.** Three-dimensional simulations in  $0.5 \text{ C}^{12} + 0.5 \text{ O}^{16}$  mixture

Run	$\rho_0$ <sup>(a)</sup>	$L$ <sup>(b)</sup>	$\left(\frac{L}{W}\right)$ <sup>(c)</sup>	$l_{max}$ <sup>(d)</sup>	$n_{1/2}$ <sup>(e)</sup>	$\left(\frac{W}{x_C}\right)$ <sup>(f)</sup>	$\left(\frac{y_p}{W}\right)$ <sup>(g)</sup>	$\left(\frac{z_p}{W}\right)$ <sup>(g)</sup>
5e5B	0.5	32.0	4	11	12.3	20.8	0.25	0.625
7e5B	0.7	6.0	4	11	12.3	41.7	0.25	0.625
1e6A1	1.0	2.0	8	12	24.5	20.8	0.25	0.5
1e6B	1.0	2.0	4	11	12.3	41.7	0.25	0.5
1e6C	1.0	2.0	8	11	12.3	20.8	0.18	0.444
1e6C1	1.0	2.0	8	12	24.5	20.8	0.18	0.444
1e6C2	1.0	2.0	8	13	49.0	20.8	0.18	0.444
1e6D	1.0	2.0	4	11	12.3	41.7	0.18	0.444

(a)  $\rho_0$  - background density in  $10^6 \text{ g cm}^{-3}$ .

(b)  $L$  - length of the computational domain in  $10^7 \text{ cm}$ .

(c)  $W$  - width of the computational domain.

(d)  $l_{max}$  - maximum level of mesh refinement.

(e)  $n_{1/2}$  - number of computational cells per a half-reaction length  $x_C$ .

(f)  $W/x_C$  - number of half-reaction lengths  $x_C$  per width  $W$ .

(g)  $y_p$  and  $z_p$  are Y- and Z-coordinates of a spherical perturbation, respectively. Radius,  $r_p = \frac{1}{4}x_C$ , and X-coordinate,  $x_p = 0.9L - \frac{2}{3}x_C$ , of a spherical perturbation are the same in all runs.

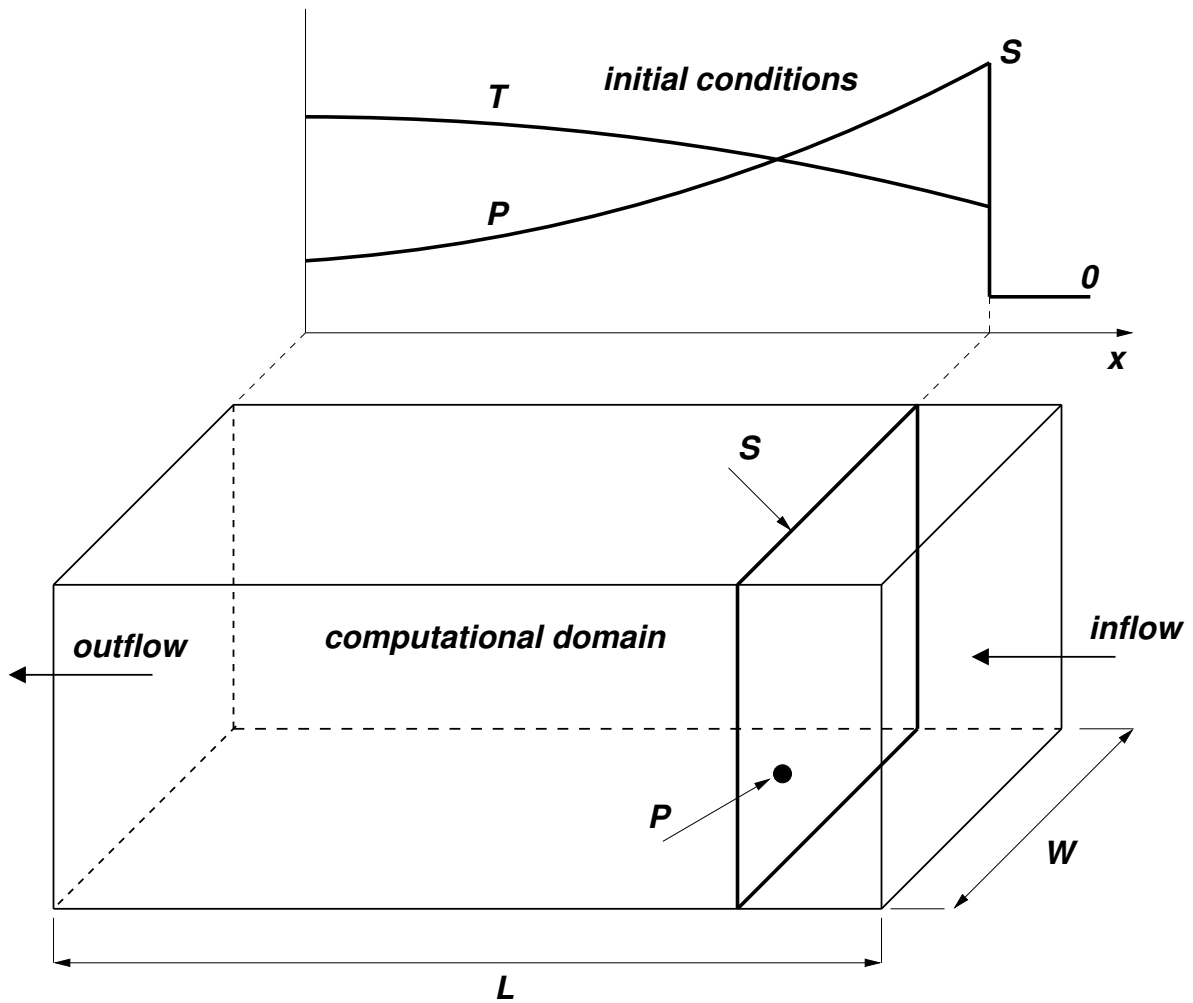


**Figure 1.** Three-dimensional computational setup (Sect. 3.2). Computational domain is a “tube” of length  $L$  and cross-section  $W \times W$ . The initial steady-state solution ( $T$  and  $P$ ) is mapped onto a mesh with the leading shock,  $S$ , facing the right  $X$ -boundary. Supersonic inflow with parameters of unburned matter and velocity  $-D$  is imposed on the right. Zero-gradient boundary conditions are imposed on the left. Symmetry boundary conditions are imposed on the  $Y$  and  $Z$ -boundaries. Spherical perturbation,  $P$ , is placed close behind the leading shock. Two-dimensional setup is the same as above but with the  $Z$ -axis removed.

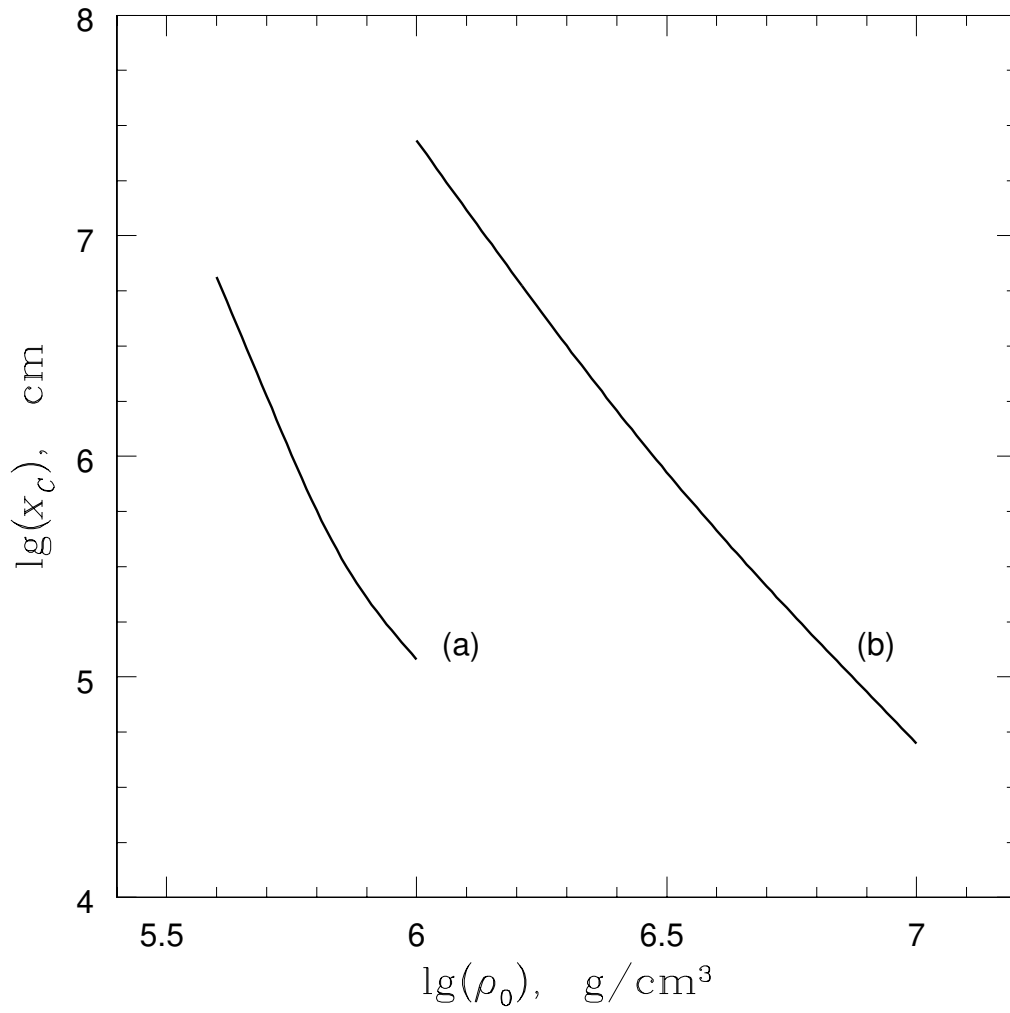


**Figure 2.** Half-reaction thickness,  $x_C$ , of a steady state one-dimensional detonation as a function of initial density  $\rho_0$  for two initial carbon mass fraction,  $X_C^{12}$ . (a)  $X_C^{12} = 0.5$  and (b)  $X_C^{12} = 0.3$ .



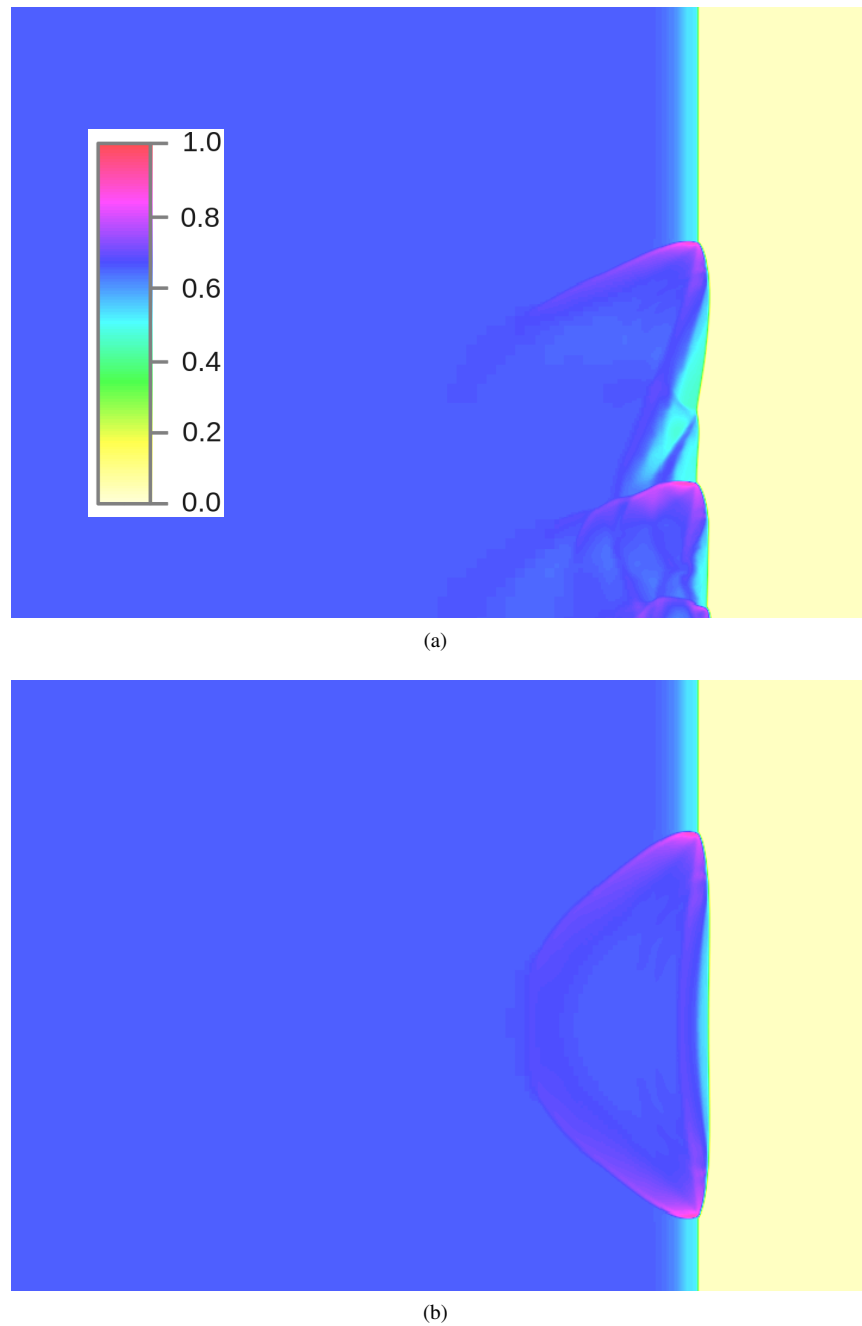


**Figure 3.** Initial stage of the development of a cellular Detonation structure in the 1e6C2 simulation run. Temperature is shown in XY (a) and XZ (b) orthogonal planes passing through the centerline of the computational domain. The temperature range is  $T = \{0 - 4 \times 10^9\}$ K. Color palette is explained in Appendix A.

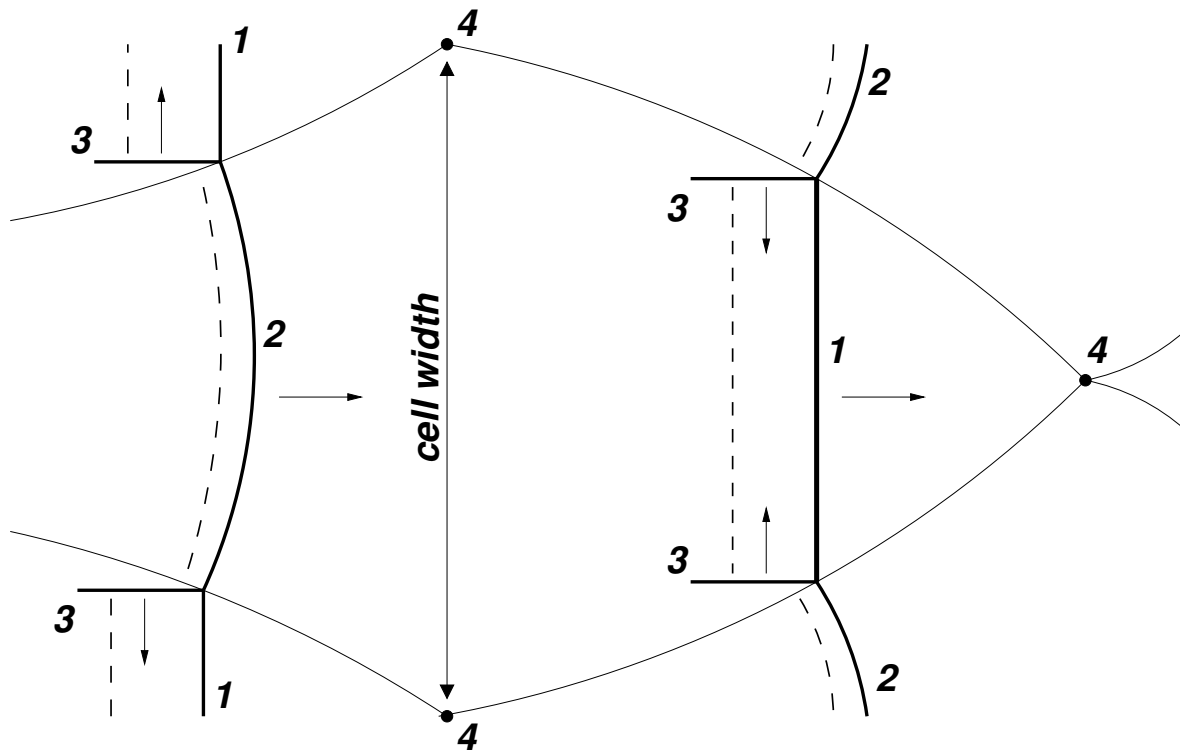


**Figure 4.** Cellular Schematics. Rhomboidal shape of a detonation cell: (1) incident waves, (2) Mach stems, (3) transversal waves and (4) collision points.

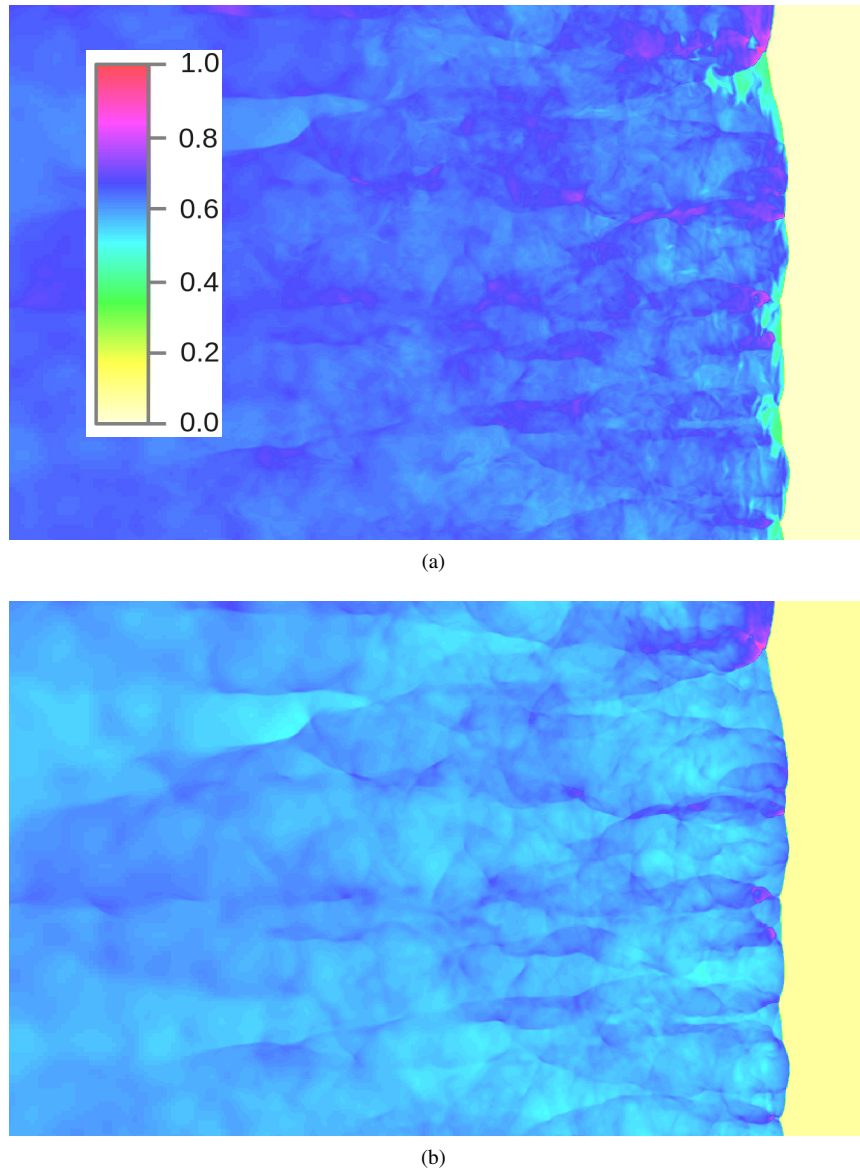


**Figure 5.** (a)  $T$  and (b)  $\lg P$  for a three-dimensional cellular detonation at  $\rho_0 = 10^6 \text{ g cm}^{-3}$  (run 1e6C2) at  $t = 50t_c$  in the XZ-plane passing through the centerline of the computational domain. The temperature and pressure range shown in the figure is  $T = \{0 - 4 \times 10^9\} \text{ K}$  and  $\lg P = \{22 - 24\} \text{ erg cm}^{-3}$ , respectively. Color palette is explained in Appendix A.

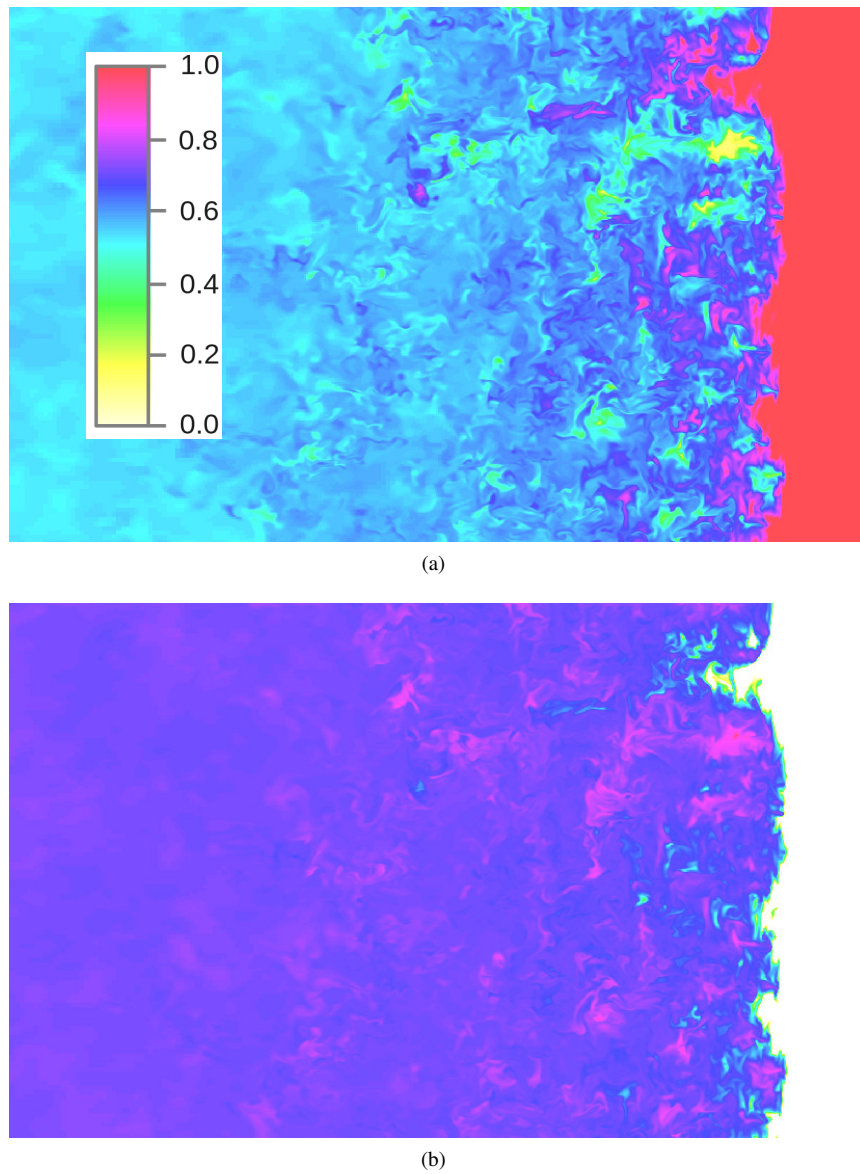


**Figure 6.** Mass fractions (a)  $X_C^{12}$  and (b)  $X_{Si}^{28}$  for a three-dimensional cellular detonation at  $\rho_0 = 10^6 \text{ g cm}^{-3}$  (run 1e6C2) at  $t = 50t_C$  in the XZ-plane passing through the centerline of the computational domain.  $X_C^{12} = \{0 - 0.5\}$ ;  $X_{Si}^{28} = \{0 - 0.6\}$ . Color palette is explained in Appendix A.

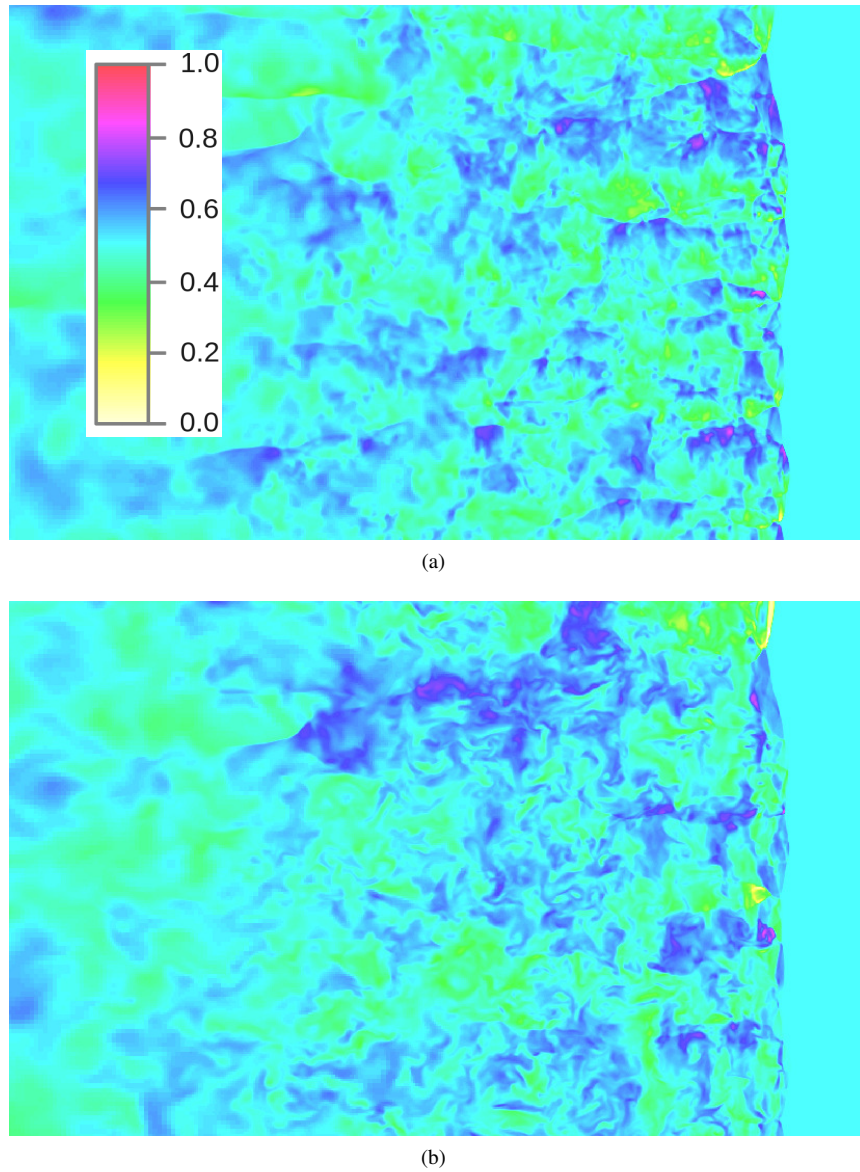


**Figure 7.** Y and Z-components, (a)  $u_y$  and (b)  $u_z$ , of a fluid velocity for a three-dimensional cellular detonation at  $\rho_0 = 10^6 \text{ g cm}^{-3}$  (run 1e6C2) at  $t = 50t_C$  in the XZ-plane passing through the centerline of the computational domain. Velocity range is  $u_{y,z} = \pm 6 \times 10^8 \text{ cm s}^{-1}$ . Color palette is explained in Appendix A.

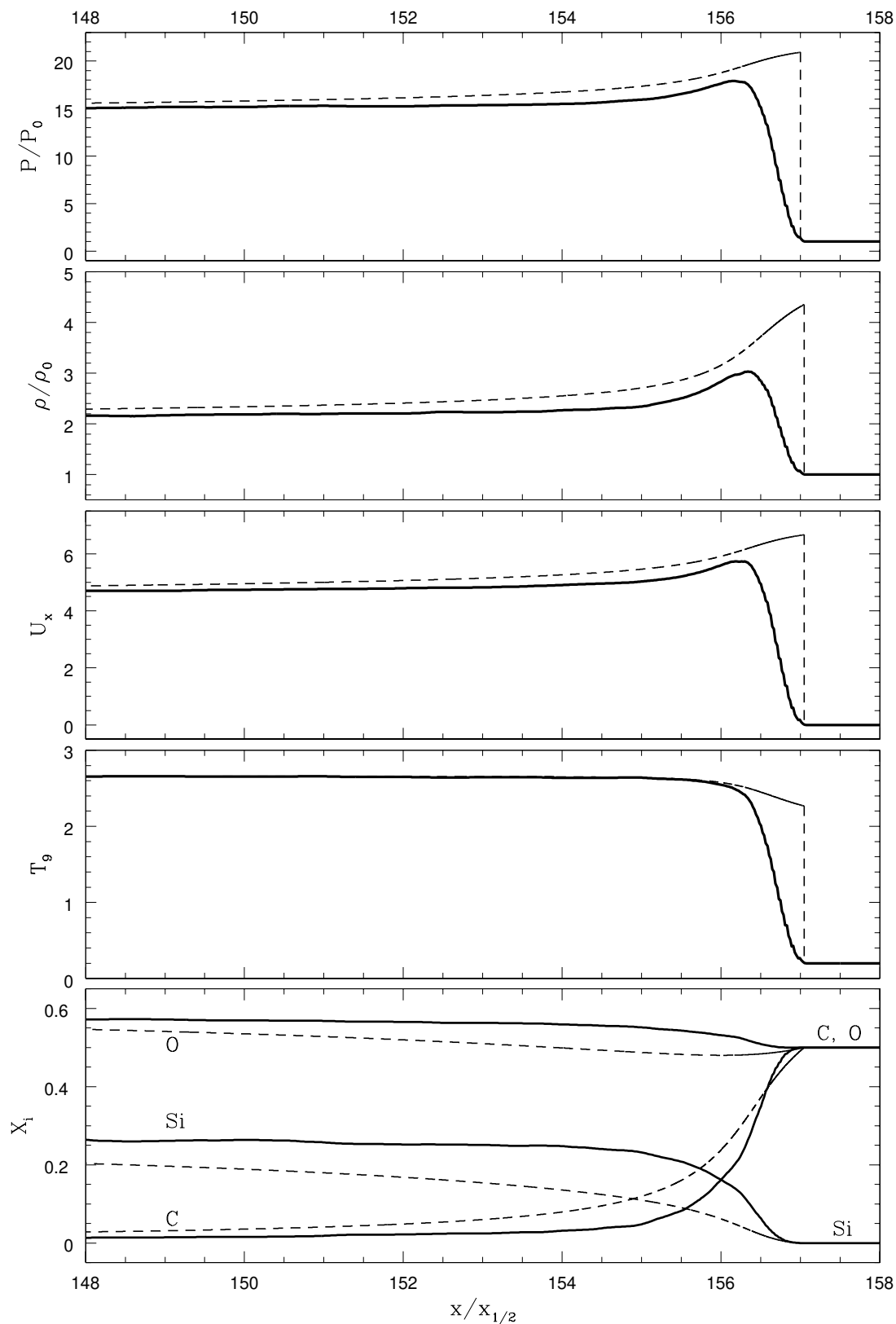


**Figure 8.** Averaged one-dimensional structure of a three-dimensional cellular CJ detonation at  $\rho_0 = 10^6 \text{ g cm}^{-3}$  (run 1e6C2) at  $t = 50t_C$ . Top to bottom: (1)  $P$ , (2)  $\rho$ , (3)  $u_x/10^8 \text{ cm s}^{-1}$ , (4)  $T/10^9 \text{ K}$ , (5)  $X_C^{12}$ ,  $X_O^{16}$ , and  $X_{Si}^{28}$  as a function of X-coordinate. Dashed lines show the corresponding steady-state solution (initial conditions).

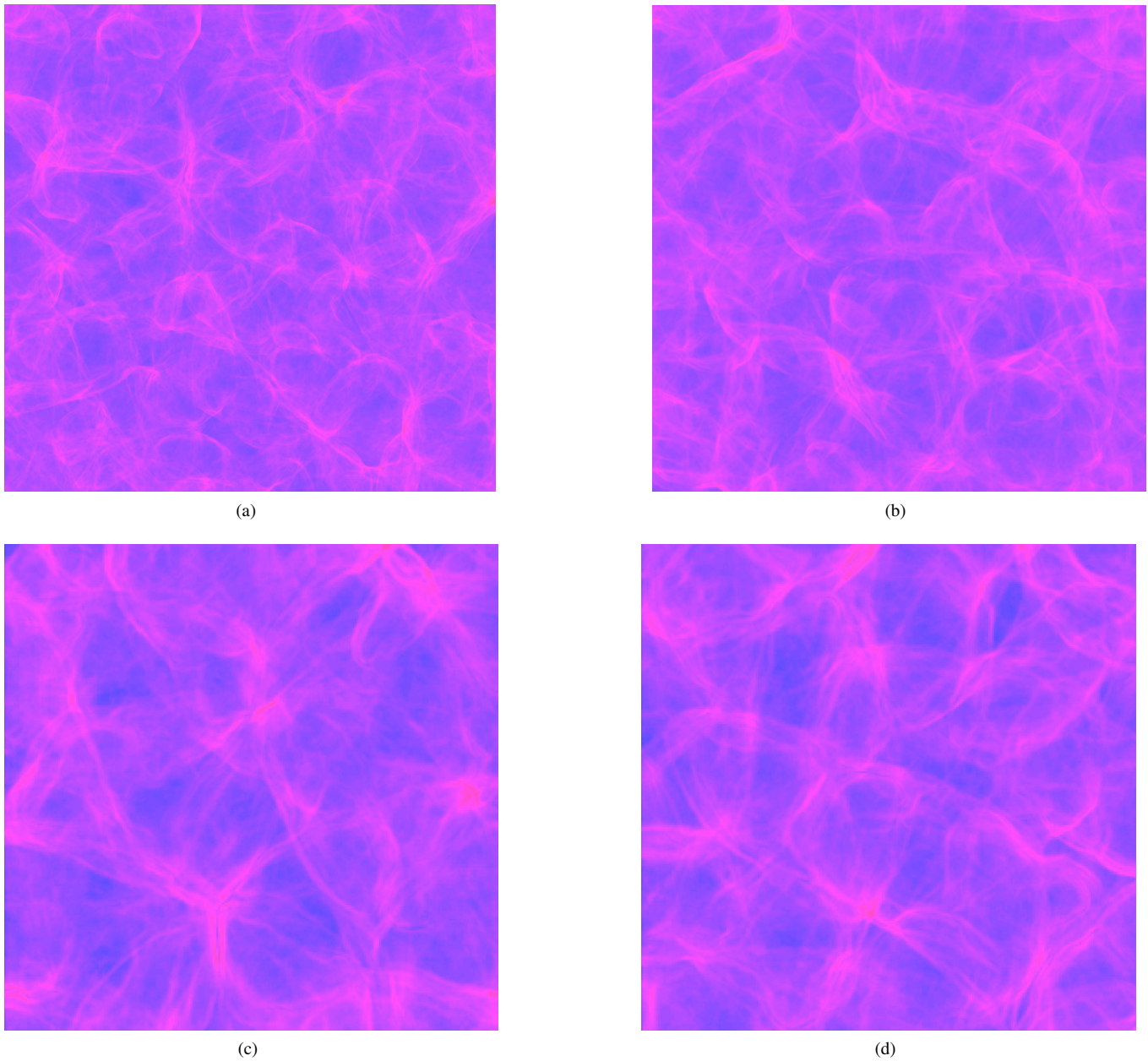


**Figure 9.** Schlieren images in the  $YZ$ -plane ( $S_x$ ) of a three-dimensional CJ cellular detonation at  $\rho_0 = 10^6 \text{ g cm}^{-3}$  from runs (a) 1e6C2, (b) 1e6C1, (c) 1e6C, and (d) 1e6D. Runs 1e6C,C1,C2 were done in the same computational domain but with different numerical resolutions  $n \approx 12.3, 24.5$  and  $49$ , respectively. Run 1e6D has the same resolution  $n \approx 12.3$  as 1e6C but was done in two-times wider tube. The frame (d) shows the lower left quarter of the 1e6D tube cross-section. The density gradient increases from blue to red.

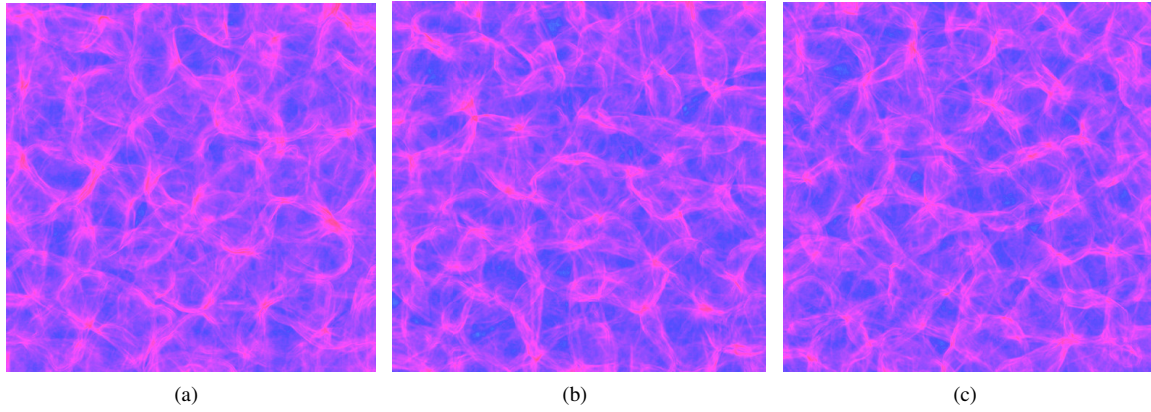
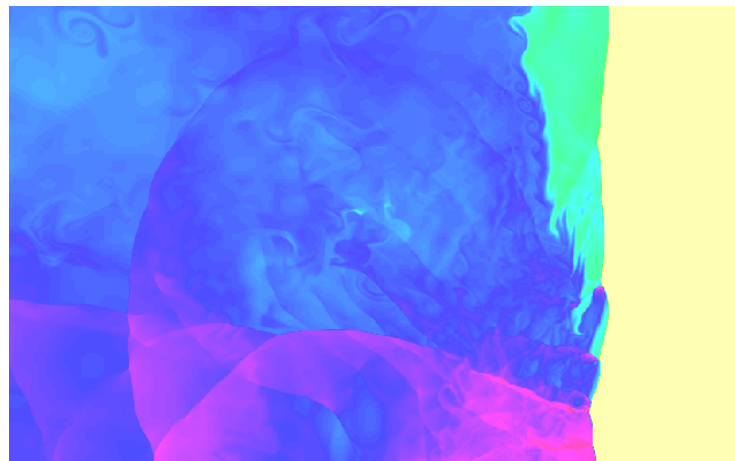
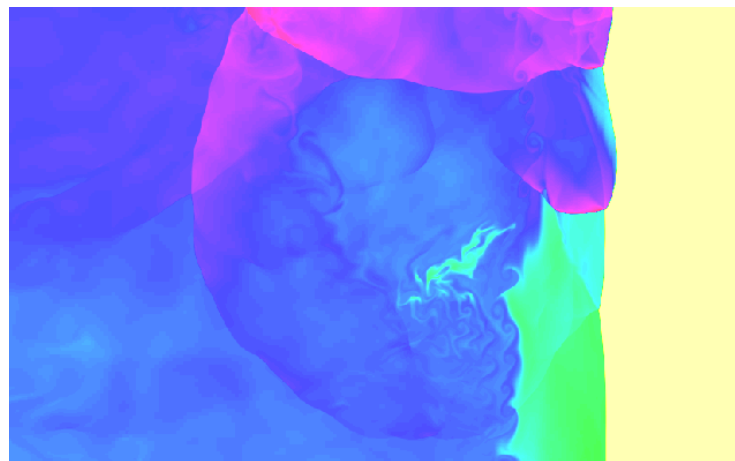


**Figure 10.** Schlieren  $S_x$  images in the YZ-plane for a three-dimensional cellular CJ detonation at different densities. (a) run 1e6D,  $\rho_0 = 10^6 \text{ g cm}^{-3}$ ,  $t = 0.046 \text{ s}$ . (b) run 7e5B,  $\rho_0 = 7 \times 10^5 \text{ g cm}^{-3}$ ,  $t = 0.091 \text{ s}$ . (c) run 5e6B,  $\rho_0 = 5 \times 10^5 \text{ g cm}^{-3}$ ,  $t = 0.49 \text{ s}$ . Detonation propagates towards the viewer. Frames are scaled to the same relative size. Values of  $t_C$  and  $W$  for the runs are given in Table. 1 and Table. 2, respectively. The density gradient increases from blue to red.

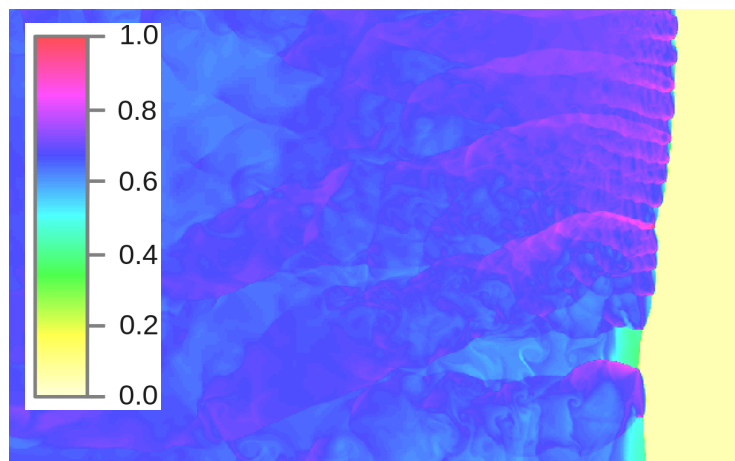




(a)



(b)



(c)

**Figure 11.** Two-dimensional cellular detonation at  $\rho_0 = 10^6 \text{ g cm}^{-3}$  (run 1e6C2-2D). The size of the computational domain is  $L=200 \text{ km}$  and  $W=25 \text{ km}$ , as for the three-dimensional run 1e6C2. Temperature is shown in the XZ-plane passing through the centerline of the computational domain. (a)  $t = 96.2t_C$ , (b)  $t = 142.3t_C$  and (c)  $t = 126.9t_C$ . The range is  $T = \{0 - 4 \times 10^9\} \text{ K}$ . Color palette is explained in Appendix A.

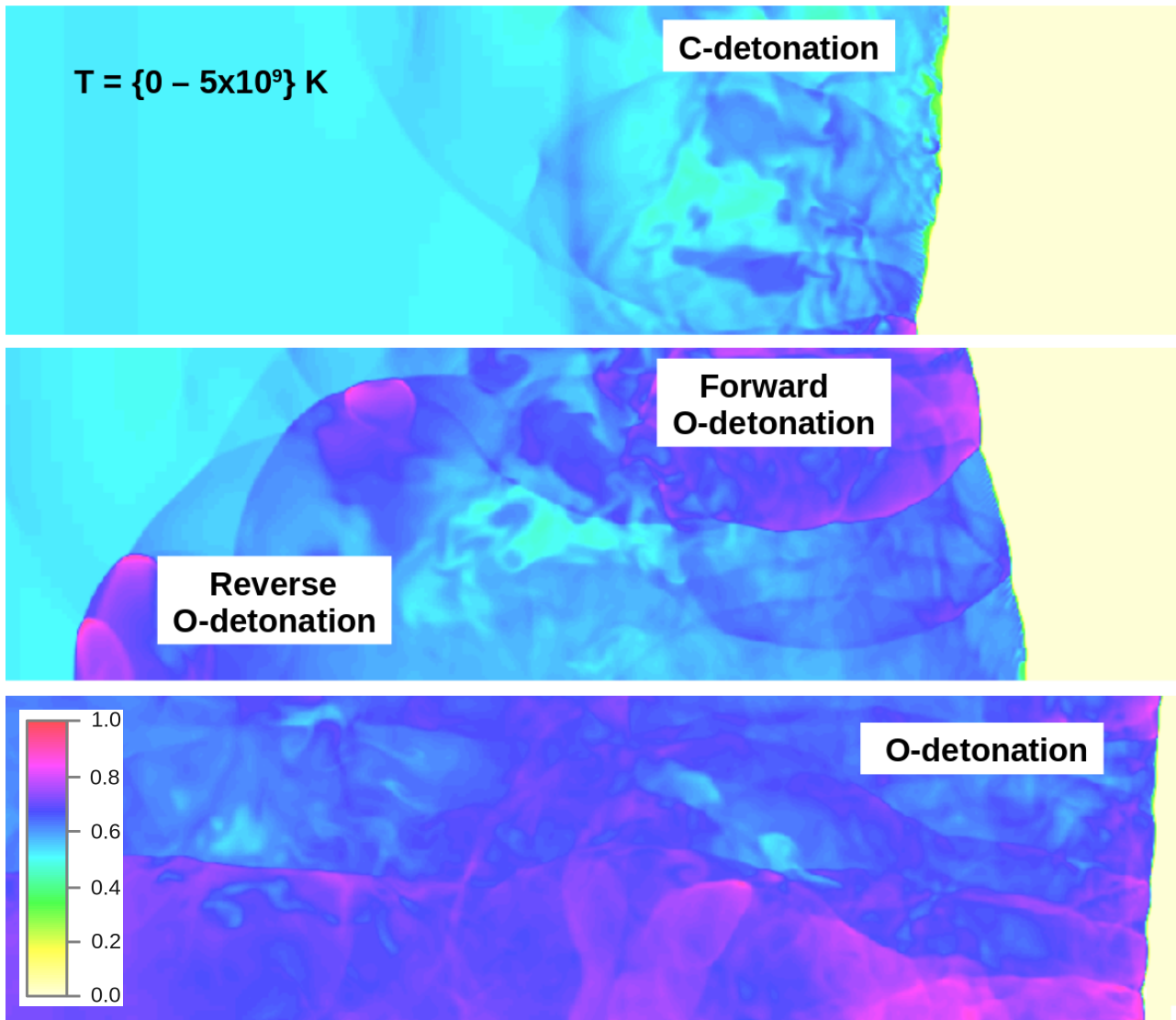


**Figure 12.** Temperature evolution of the detonation front for 0.3 C and 0.7 O mass fraction, at  $\rho_0 = 10^6 \text{ g cm}^{-3}$  (similar to run 1e6C2) for  $t=50, 123$  and  $223 t_C$  in the XZ-plane passing through the centerline of the computational domain.  $T = \{0 - 5 \times 10^9 \text{ K}$ . Color palette is explained in Appendix A. The rapid transition to explosive O-burning results in high temperatures.

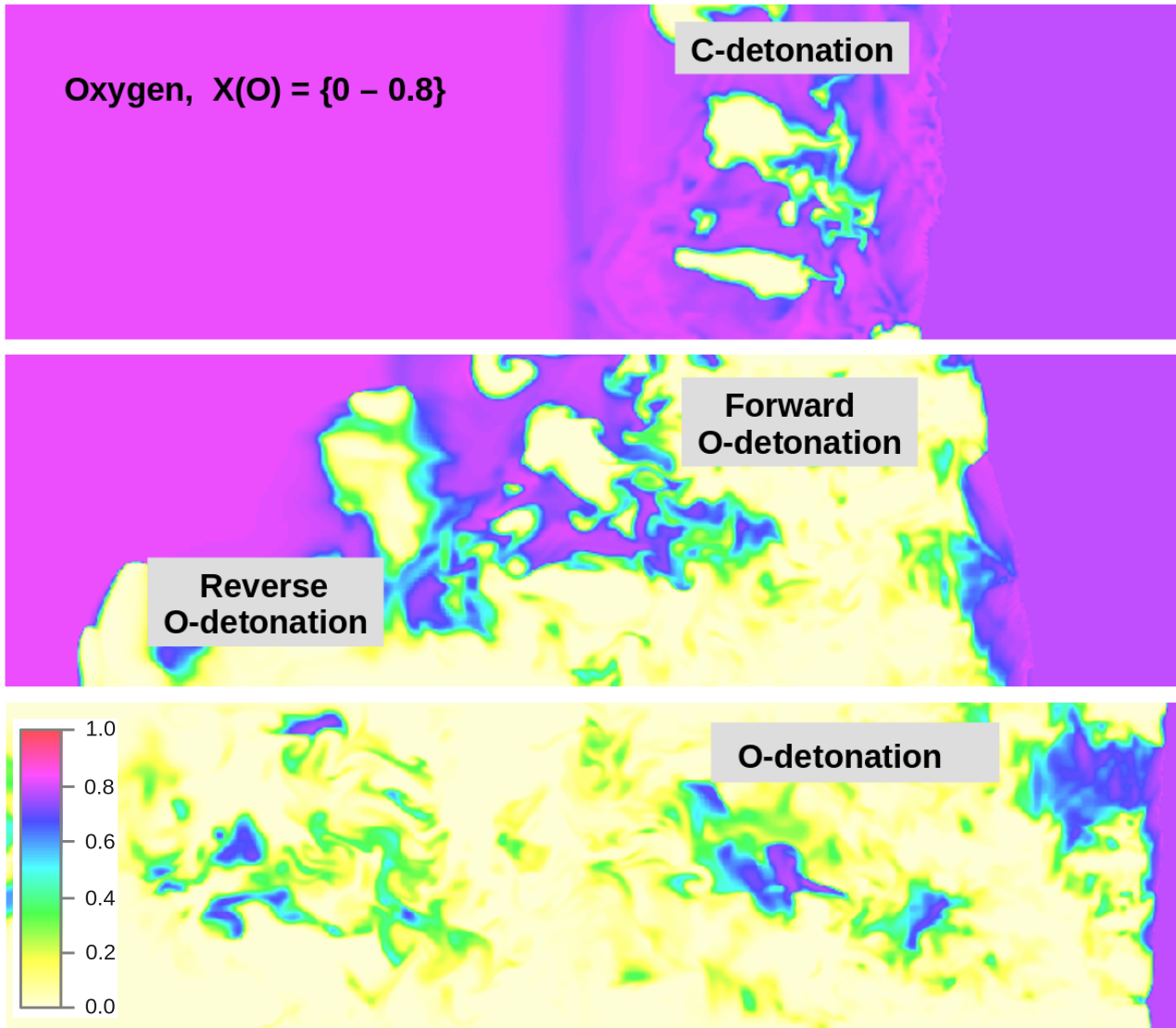


**Figure 13.** Mass fraction of  $X_O^{16}$ , same as Fig. 12.  $X_O^{16} = \{0 - 0.8\}$ . Color palette is explained in Appendix A

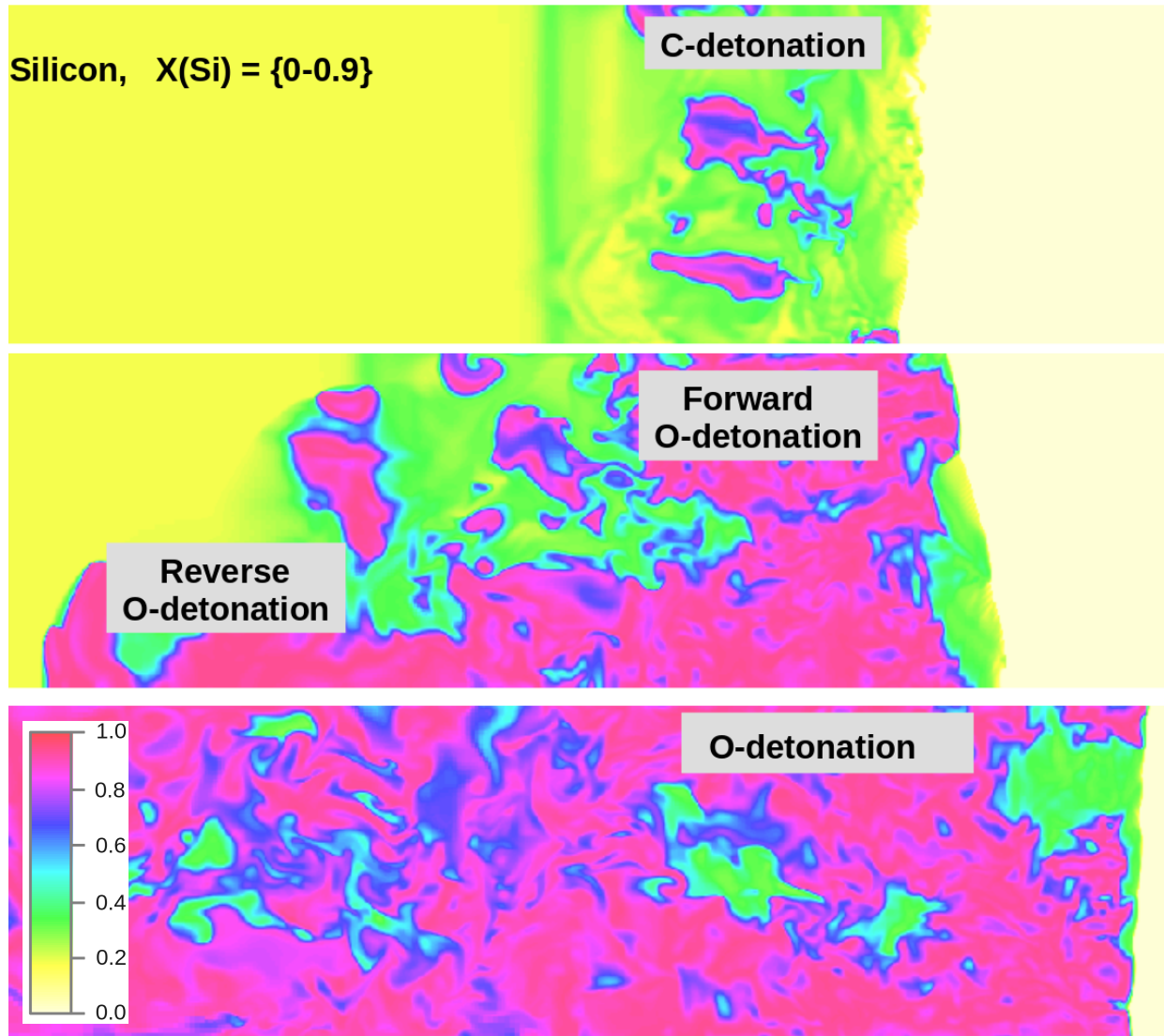


**Figure 14.** Mass fraction of  $X_{\text{Si}}^{28}$ , same as Fig. 12.  $X_{\text{Si}}^{28} = \{0 - 0.9\}$ . Color palette is explained in Appendix A

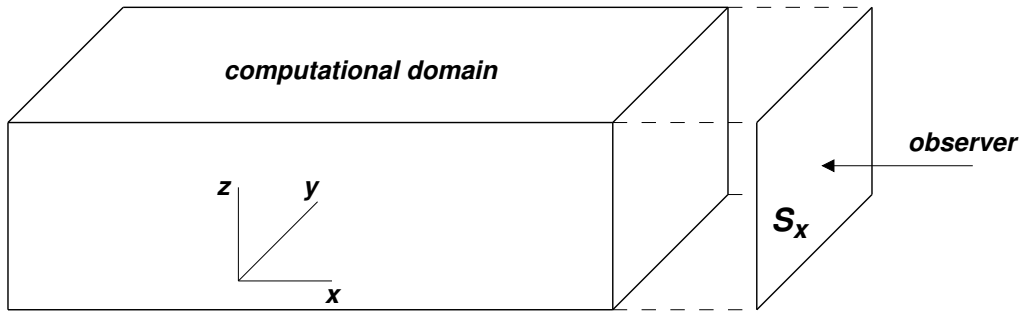


**Figure 15.** Schematic of Schlieren visualization. Detonation propagates through the computational domain from left to right. A frontal (head-on) Schlieren image  $S_x$  is generated by integrating along the X-axis of an absolute value of the orthogonal component of the density gradient, Equation (A2).